International Journal of Disaster Risk Reduction 90 (2023) 103610

Contents lists available at ScienceDirect

International Journal of Disaster Risk Reduction

journal homepage: www.elsevier.com/locate/ijdrr

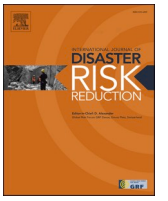

Assessing the potential implementation of earthquake early warning for schools in the Patras region, Greece

Carmine Galasso [a,b,*], Elisa Zuccolo [c,d], Karim Aljawhari [a,b], Gemma Cremen [a], Nikolaos S. Melis [e]

[a] University College London (UCL), Department of Civil, Environmental, and Geomatic Engineering, London, UK
[b] Scuola Universitaria Superiore (IUSS) Pavia, Centre for Training and Research on Reduction of Seismic Risk (ROSE), Pavia, Italy
[c] European Centre for Training and Research in Earthquake Engineering (EUCENTRE), Dept of Risk Scenarios, Pavia, Italy
[d] Istituto Nazionale di Oceanografia e di Geofisica Sperimentale (OGS), Seismological Research Center (CRS), Udine, Italy
[e] National Observatory of Athens (NOA), Institute of Geodynamics, Athens, Greece

ARTICLE INFO

Keywords:
Earthquake early warning
Greece
Schools
Warning Time
Decision-making

ABSTRACT

Earthquake early warning (EEW) is currently deemed a credible approach to seismic resilience enhancement in modern societies, especially if part of a more holistic earthquake mitigation strategy involving other risk reduction tools such as structural upgrading/retrofit. Yet, there remains a strong need to 1) assess the feasibility of EEW in various seismotectonic contexts, considering specific target applications/end users; and 2) develop next-generation decision-support systems relying on interpretable probabilistic impact-based estimates toward more risk-informed decision-making on EEW installation/alert triggering. These challenges are addressed in this paper, which showcases a series of recent significant EEW contributions by the authors. First, we present the results of a state-of-the-art feasibility study for EEW in schools performed across the Patras region of Greece, attempting to spatially combine traditional seismologically-driven EEW decision criteria (i.e., warning time) with proxy risk-oriented measures for earthquake impact (i.e., building fragility and the number of exposed school students). These results show that, under certain conditions, EEW could be effective for the schools in the considered case-study region. We then demonstrate an advanced end-user-centred approach for improved risk-informed decision-making on triggering EEW alerts. The proposed methodology integrates earthquake-engineering-related seismic performance assessment procedures and metrics with multi-criteria decision-making (MCDM) within an end-to-end probabilistic framework. The performance-based earthquake engineering component of such a framework facilitates the computation of various damage/loss estimates (e.g., repair cost, downtime, and casualties) by combining target-structure-specific models of seismic response, fragility, and vulnerability with real-time ground-shaking estimates. Additionally, the incorporated MCDM methodology enables explicit consideration of end-user preferences (importance) towards the estimated consequences in the context of alert issuance. The developed approach is demonstrated using an archetype school building for the case-study region, for which we specifically investigate the optimal decision (i.e., "trigger" or "don't trigger" an EEW alert) across a range of ground-motion intensity measures. We find that the best action for a given level of ground shaking can vary as a function of stakeholder preferences.

* Corresponding author. University College London (UCL), Department of Civil, Environmental, and Geomatic Engineering, London, UK.
E-mail address: c.galasso@ucl.ac.uk (C. Galasso).

https://doi.org/10.1016/j.ijdrr.2023.103610
Received 29 August 2022; Received in revised form 20 February 2023; Accepted 20 February 2023
Available online 26 February 2023

1. Introduction

Earthquake early warning (EEW) systems detect earthquakes in the initial phases of fault rupture, rapidly estimate source parameters and/or the intensity of the resulting ground motion, and alert end users before they experience the intense shaking that might cause damage and financial/human losses. A review of worldwide EEW applications shows that the warning time facilitated by an EEW system (typically seconds to tens of seconds, depending on the source-to-site distances) can potentially reduce the impact of an earthquake across many sectors of society, although inherent, practical limitations exist (e.g., [1–3]).

Progress in engineering-oriented research and development in EEW has been slow, in sharp contrast to the rapid EEW advancements that have been achieved in the seismology community (e.g., [4,5]). From an engineering perspective, the first step is to estimate source parameters and/or ground-motion intensity measures (IMs), outputs of traditional EEW systems [6,7]. These real-time estimates should be combined with next-generation decision-support tools that incorporate advanced risk-based predictions of earthquake-induced consequences on buildings/infrastructure to determine whether mitigation actions should be triggered, leading to more informed EEW alert issuance (e.g., [4]). This end-to-end engineering-oriented approach to EEW was recently achieved in [8], within the context of the state-of-the-art performance-based earthquake engineering (PBEE) framework [10]. This framework can be used to estimate the seismic performance of buildings, infrastructure components, and other built assets in terms of consequence metrics of interest to end users (i.e., "dollars, deaths, and downtime"). The methodology introduced in [8] specifically leverages the PBEE-based early warning (PBEEW) framework developed in [11]. It combines its risk-based estimates with multi-criteria decision-making tools to investigate optimal EEW decisions (i.e., "trigger"/"do not trigger" alerts).

Ref. [12] revealed that typical EEW end-user systems are hospitals, public transportation systems, and schools. EEW can be particularly beneficial for schools, where the consequences of false alarms (i.e., erroneous triggering of EEW alerts) are not costly. The potential risk-mitigation rewards in terms of life safety and long-term education support are substantial. Ref. [13] states "*Although it is generally not recommended to run outside of buildings in a city in case of earthquakes because of falling debris, schools may be successfully evacuated because open areas for recreation and sports surround them. Also, in some earthquake-prone regions, like Lima, Peru, most schools have only two floors, allowing evacuation in 5*–15 s". Many previous studies have considered school facilities as potential targets for EEW in various parts of the world (e.g., [14–17]). For instance, Ref. [18] investigated EEW feasibility for schools in the Campania region (southern Italy). The study considered potential earthquake sources for the area, the Italian accelerometric network as the recording network for seismic events, and the performance of the software platform *PRESTo*^{Plus} (a network-based EEW system developed by the same research group) for data analysis and processing. The authors concluded that an efficient EEW system could enable most schools in the region to undertake some mitigating actions for an incoming event. However, none of the existing literature on EEW applications in schools has considered an engineering-oriented approach, which this paper attempts to address.

This study specifically investigates risk-oriented EEW feasibility for schools in the region of Patras, Greece. It also implements the risk-informed EEW decision-making methodology proposed in [8] for an archetype school building in the same region. Patras is Greece's third-largest city and the regional capital of Western Greece. The entire Patras Gulf area is part of one of the testbeds considered in the framework of the European Union's Horizon 2020 research and innovation program "*TURNkey - Towards more Earthquake-resilient Urban Societies through a Multi-sensor-based Information System enabling Earthquake Forecasting, Early Warning and Rapid Response actions*" (https://earthquake-turnkey.eu/, last accessed February 2023). Southeastern Europe is the continent's most seismically active region, with Greece, Italy, and Turkey often experiencing the most frequent and strongest earthquakes. However, Greece (and Italy) do not currently have operational government-supported, country- or region-wide EEW systems in place (although the Android Earthquake Alert System, which uses Android phones to issue and receive early warnings, has recently been launched in Greece; e.g., [19]).

The general feasibility of EEW in Europe, and specifically in Greece, has recently been demonstrated in [9]. This study calculated the amount of warning (or lead) time (i.e., the time between the delivery of an EEW alert and the arrival of shaking at target sites, including various technical/operational delays) that might be possible at multiple locations across Europe exposed to significant seismicity, based on the locations of 2377 sensor stations. The computed lead times were combined with estimates of the expected level of shaking (in terms of the European Macroseismic Scale (EMS)-98 seismic intensity scale, specifically designed for European countries) and the number of people potentially affected. This information, together with an estimate of the accuracy of the warning, led to a new relative indicator (i.e., EEW relative feasibility index) for the potential usefulness of EEW across Europe. This index revealed that parts of the Euro-Mediterranean region could benefit from EEW and its potential for mitigating the detrimental effects of earthquakes.

We refine the approach used in [9] by investigating EEW feasibility for schools in Patras, overcoming some of the simplifying assumptions of the Europe-wide study that mainly relate to 1) the use of continent-wide, open data and tools – to ensure consistency of application across Europe; and 2) the working assumption that the considered seismic stations are (or could be) capable of being used for EEW purposes (i.e., they have or could have adequate data acquisition/transmission systems, real-time communication capability, robust dissemination methods, power supply systems, etc.). In particular, our lead-time analyses account for several EEW (i.e., regional vs onsite) and seismic network configurations, different types (and numbers) of seismic sensors available in the region (i.e., broadband and short-period sensors, as well as low-cost accelerometric ones) and the disaggregation of lead times by various seismic sources (as well as potential earthquake magnitudes of interest). Our feasibility analysis in this paper also explicitly considers the physical vulnerability of an archetype school building in the case-study region – through a state-of-the-art modelling approach – and therefore is a more rigorous risk-oriented approach.

The paper is organised as follows. First, we introduce the case study region, focusing on the seismotectonic and seismic monitoring of the area. Then, we evaluate the EEW feasibility for school buildings in Patras, which first involves defining a representative archetype structure based on rapid visual survey results. Detailed fragility analysis results for the selected archetype school building

are used together with lead time estimates to define an EEW relative feasibility index for Patras schools, also accounting for student exposure in each school. Finally, we demonstrate the engineering-oriented EEW approach of [8] for the archetype school building.

2. Case-study region

The region surrounding Patras (Fig. 1), which corresponds to the TURNkey Testbed region in Greece, is dominated by a highly seismically active normal fault zone of an almost east-southeast - west-northwest strike direction. This zone is linked via a transtensional northeast-southwest zone from the Corinth Gulf (to the east) to the west of Patras Gulf (e.g., [28–30]). The western Gulf of Corinth experiences extensional seismic activity near and around the town of Aegion, which damaging earthquakes have hit since historical times (e.g., [31]). The latest damaging event, which occurred on June 15, 1995, with a moment magnitude (M_W) of 6.4 [32], devastated Aegion and surrounding regions, with severe damage occurring to the building stock, including the collapse of two reinforced concrete multi-story buildings (i.e., a hotel and an apartment complex). The two collapses resulted in 26 casualties (e.g., [33, 34]). The Patras Gulf transtensional fault boundary is connected with branches of smaller east-west normal fault structures (i.e., Agia Triada fault in Patras city; [35]). It continues towards the south to a strike-slip fault activated by the M_W 6.4 earthquake on June 8, 2008 (e.g., [36]). This event devastated the rural area southeast of Patras city, causing significant damage predominantly to weak structures in villages and small towns south of Patras.

Located west of the Testbed region is Greece's zone of highest seismic hazard, containing the central Ionian Islands (namely Kefalonia, Zakynthos, and Lefkada). This zone is dominated by extreme events with magnitudes larger than 7.0 that have produced moderate-to-high structural and nonstructural damage in Greece (e.g., [37]). It lies at the transition between the north-south extension of central Greece (from the Gulf of Corinth to the last western extensional feature, the Gulf of Patras, from east to west) to the transfer fault of the Ionian Islands that links the African subduction zone (along the Hellenic Arc) with the Apulian Collision to the north [38].

The region considered in this study is monitored by the Hellenic Unified Seismic Network (HUSN), which is managed by the National Observatory of Athens (NOA) and acts as an operational seismic network to monitor earthquake activity in Greece and the adjacent region, informing the Greek State and the general public. Fig. 1 also shows the stations available in real-time via HUSN and the European Integrated Data Archive (EIDA) NOA node,[1] which provides open data for research purposes. They include both weak - (short period and broadband) and strong-motion sensors and belong to the seismic networks operated by NOA (HL), University of Patras (HP), University of Athens (HA), University of Thessaloniki (HT), Institute of Engineering Seismology and Earthquake Engineering (HI), and the Corinth Rift Laboratory - Center National de La Recherche Scientifique (CL).

During the TURNkey project, low-cost accelerometric sensors were deployed in November 2019 to densify the existing network in Patras, Aegion, and Kalavrita, in the greater Achaia prefecture. The stations of the TURNkey project currently comprise 40 Raspberry-Shake 4D (RS4D) sensors[2] (low-cost accelerographic devices) and 13 *P*-Alert sensors[3] (low-cost accelerographic devices), which are located inside schools and public buildings. A dedicated website[4] provides information on their everyday operation; this strong-motion network is linked to the TURNkey FWCR (Forecasting - Early Warning - Consequence Prediction - Response) platform. The latter is a comprehensive information system facilitating operational earthquake forecasting, regional earthquake early warning, and post-earthquake rapid response actions across the European continent. TURNkey network stations considered for this study are shown in Fig. 1.

In this study, we focus on the 268 schools located in Patras city and the broader Municipality of Patras. The considered schools include both public and private schools, spanning several student age levels from kindergarten to high school, as retrieved from open data published by the central Greek government.[5]

3. Archetype school building: geometry, materials, and modelling

The current study adopts the methodology proposed in [8] to establish a risk-informed EEW decision support system for an archetype school building in Patras. Similarly to [39] (among others), the archetype was identified by carrying out a remote rapid visual survey to investigate the prevalent geometric characteristics (i.e., plan shape, number of storeys, approximate floor height, number of bays, and approximate span lengths in both horizontal directions) of school buildings in Patras. The survey incorporated a subset of 45 different schools in the city of Patras, comprising a total of 61 buildings. Due to the COVID-19 pandemic and travel restrictions during the study, these buildings were virtually inspected through Google Maps/Street View,[6] also considering information available on the web via the Greek Ministry of Education, Research, and Religious Affairs,[7] in addition to the 2001 census carried out by Hellenic Statistical Authority.[8]

A summary of the information collected via the remote visual survey is visualised in the pie charts in Fig. 2. Most inspected school buildings are rectangular in terms of plan shape (almost 51%) and are composed of two storeys (about 60%), according to Fig. 2a and b, respectively. Moreover, Fig. 2c demonstrates that an approximate height of 3.5 *m* characterised around 61% of the storeys across all

[1] https://eida.gein.noa.gr/.
[2] https://raspberryshake.org.
[3] http://www.sanlien.com.tw/product/palert.
[4] https://accelnet.gein.noa.gr/TURNkey/.
[5] https://data.gov.gr.
[6] https://maps.google.com.
[7] http://www.ermis.gov.gr.
[8] https://www.statistics.gr.

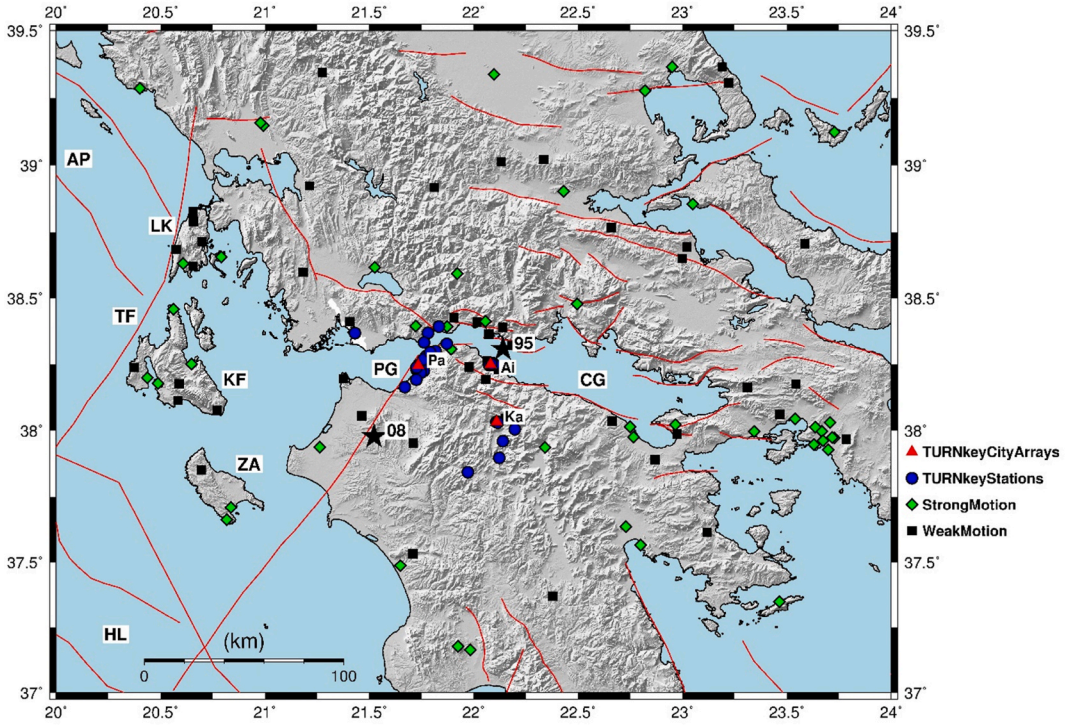

Fig. 1. Seismic stations considered in the study. Black solid stars indicate the two epicentres of the 1995 and 2008 events mentioned in the text. The double black capital letters are acronyms that stand for: Gulf of Patras (PG), Gulf of Corinth (CG), Ionian Islands (Zakynthos (ZA), Kefallonia (KE), Lefkada (LK)), the Hellenic Arc (HL), the Apulian Collision (AP), and the Ionian Islands Transfer Fault (TF). The elevation data represented in the map is taken from Shuttle Radar Topography Mission (SRTM) 1 Arc-Second Global ([20]) and the red fault lines from the Greek Database of Seismogenic Sources (GreDaSS; [21]). Symbols listed in the legend represent the existing stations available through the Hellenic Unified Seismic Network (HUSN; strong-motion stations are marked by green diamonds, while weak-motion stations - broadband and short period - are marked by black squares). The stations belong to the following seismic networks: HL [22]; HT [23]; HP [24]; HA [25]; HI [26]; CL [27]. Red triangles identify the TURNkey arrays in Patras city (Pa), Aigion town (Ai) and Kalavrita town (Ka), while blue circles represent the other TURNkey stations.

buildings. The survey also indicates that the number of bays in the longitudinal direction is scattered between three and 19 (there are no dominant values). However, the most frequent bay numbers are three, four, five, eight, and 11, as per Fig. 2d. Conversely, Fig. 2e shows that the number of bays in the short direction is predominantly two, in 53% of the investigated buildings (Fig. 2e). Lastly, 44% of the school buildings have an approximate span length of 3.5 *m* in the longitudinal direction, as indicated in Fig. 2e. In contrast, the span lengths in the short direction are more evenly distributed, as observed in Fig. 2g.

The summary of geometric characteristics enables an archetype (or index) structure to be identified that broadly reflects the general practice of schools' design/construction in the Patras region. The geometry of the developed archetype structure is based on the dominant characteristics observed in Fig. 2 without explicitly accounting for their correlation (which is generally low based on the visual inspection of the considered schools). Accordingly, the resulting structure is rectangular in plan and is composed of two storeys with a height of 3.5 *m* each. There are nine bays in the longitudinal direction, with a uniform bay length of 3.5 *m*; three bays with a length of 4.0 *m* for the classrooms and 2.0 *m* for the corridor are assumed in the short direction of the building. This results in an overall longitudinal plan dimension of 31.0 *m*, a short plan dimension of 10.0 *m*, and a total floor area of 310 m.^{2} Each floor comprises four classrooms with an area of 56 m^2 each, a staircase, and a 2.0m-wide corridor extending along the longitudinal direction of the floor. These geometric features are illustrated in Fig. 3, which provides a plan view of the developed archetype building.

The age of construction (or of significant retrofit) is another important parameter that could provide information on the type of lateral load-resisting system, construction practice, and seismic design provisions (if any) implemented in the design and construction of a building. However, this type of information cannot be captured by the remote visual survey approach adopted in this study. As Greece is characterised by moderate-to-high seismic activity, we assume that the developed archetype building complies with some modern seismic design requirements. It is acknowledged that some non-code-conforming school buildings still exist in Greece; yet, considering EEW applications for these cases might not be desirable. This is because non-code-conforming educational facilities could incur severe structural and nonstructural damage or even local/global collapses under intense ground shaking. This would diminish the benefits of practical actions (e.g., "drop, cover, and hold on" - DCHO - or move to safer locations within the building) that can be taken by people when an EEW system issues an alert during an earthquake. In fact, EEW systems are arguably only effective as part of a holistic seismic risk mitigation strategy, which also incorporates upgrading the performance of existing structures to modern/current building codes that reduce their seismic vulnerability (e.g., [3]).

We specifically assume that the archetype school building follows the latest seismic design requirements of Eurocode 8 [40]. We perform a simulated design procedure to determine the required detailing (i.e., reinforcement) and cross-section dimensions,

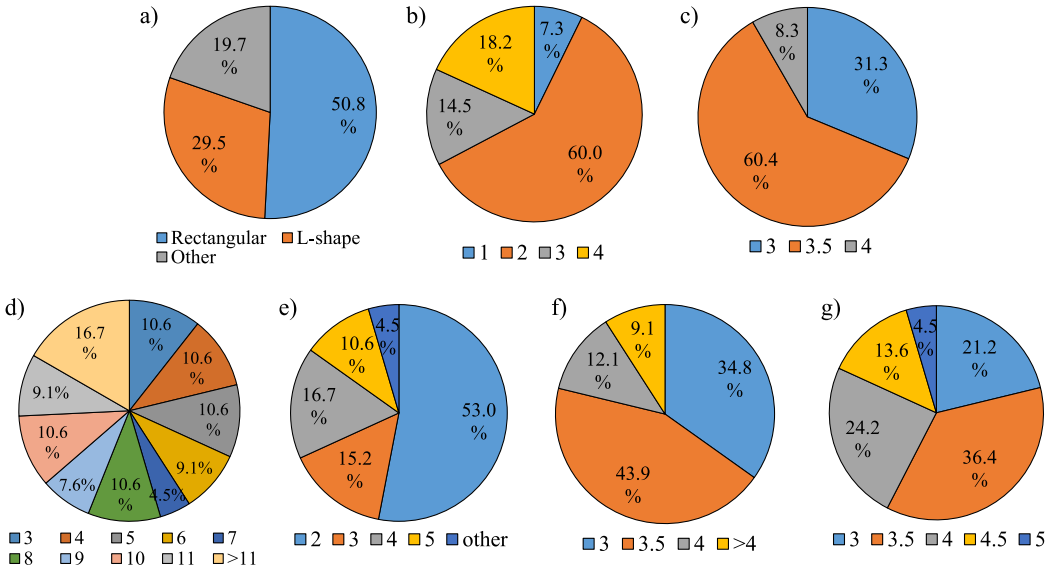

Fig. 2. Summary of the surveyed schools with respect to the following geometric characteristics: a) plan shape; b) number of storeys; c) approximate floor height in m; d) number of bays in the longitudinal direction; e) number of bays in the short direction; f) approximate bay length in the longitudinal direction (in m); and g) approximate bay length in the short direction (in m).

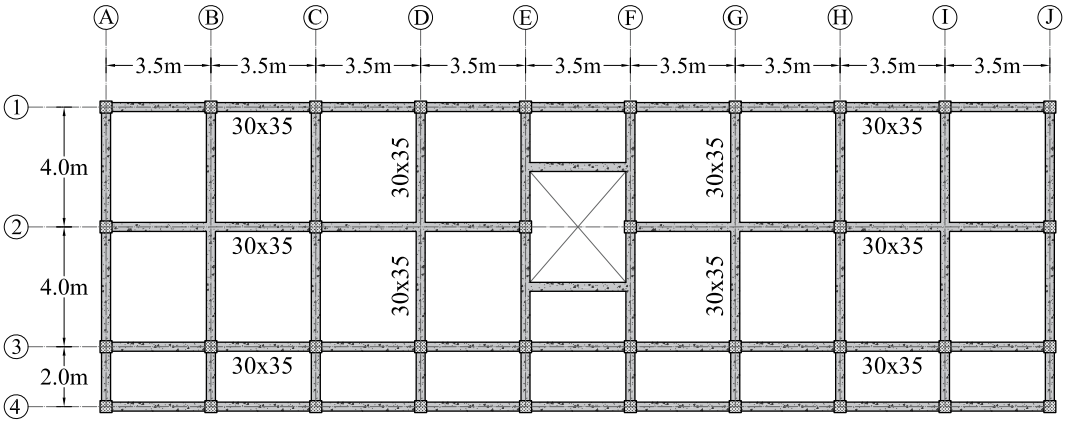

Fig. 3. Plan view of the developed archetype school building. Section dimensions are in cm.

considering the provisions of high-ductility-class structures. These provisions require capacity design, strong-column-weak-beam design, high confinement of columns, and joint reinforcement, ensuring the structure exhibits an overall ductile beam-sway (global) mechanism, preventing local brittle failure modes/global collapse. The design seismic load for the ultimate limit state, which corresponds to a 10% probability of exceedance in 50 years, is described by the Type 1 elastic response spectrum in Eurocode 8. We consider a peak ground acceleration (PGA) of 0.43 g [41] and ground type C [35]. We also adopt typical average values for the concrete compressive strength (f_{cm}) and reinforcement yield strength (f_{ym}), which are equal to 33 MPa and 544 MPa, respectively [42]. The gravity loads include a uniformly distributed live load of 2.5 kPa [43] and a superimposed dead load equal to 1.0 kPa, along with the self-weight of structural and nonstructural components.

Fig. 4 shows the resulting elevations and dimensions of structural components for Frame 3-3 in the longitudinal direction and Frame B–B in the transverse direction, in addition to cross-section samples for both beams and columns. The archetype structure incorporates masonry infill walls composed of hollow clay bricks, which is standard construction practice in the Mediterranean region. Such infill walls are among the major contributors to earthquake-induced direct economic losses, especially after minor-to-moderate ground-shaking events. They can significantly affect the seismic performance of the structure due to infill-frame interaction (e.g., [44,45]). The average mechanical properties of the infill walls implemented in the current study are summarised in Table 1 (e.g., [46,47]). We simulate the nonlinear response of the archetype school building via 2D numerical models developed using OpenSees software [48,49]. Details of the adopted nonlinear modelling strategy are provided in Appendix A.

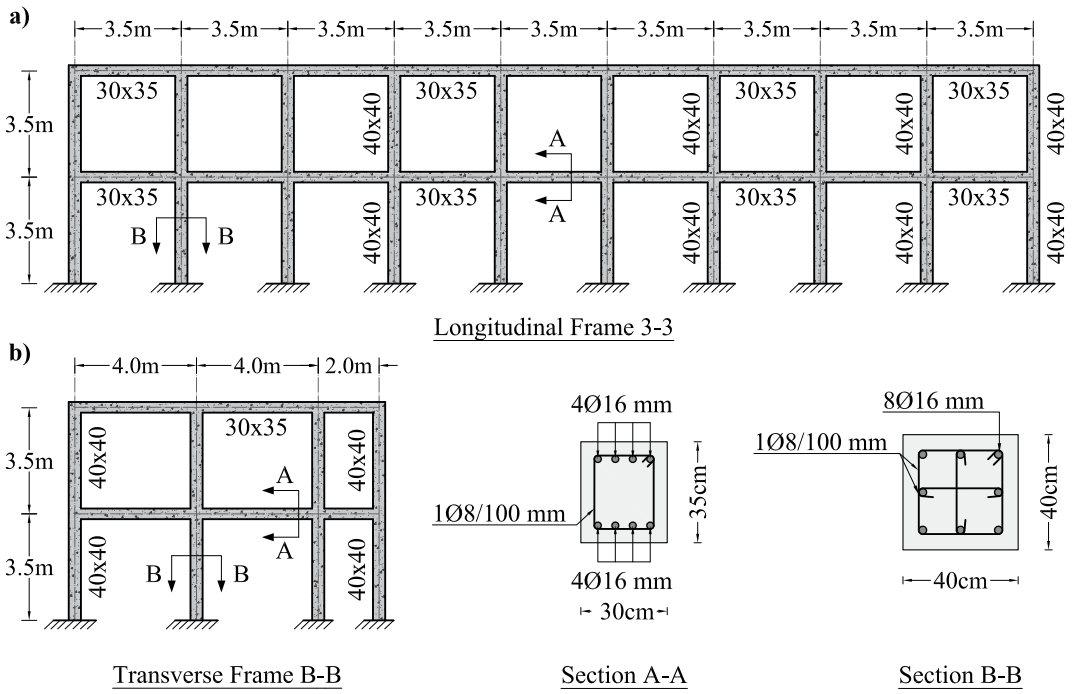

Fig. 4. Elevation of (a) Frame 3-3 in the longitudinal direction; and (b) Frame B–B in the transverse direction. Section dimensions are in cm.

4. Seismic fragility analysis

Investigating the feasibility of implementing an EEW system for schools in Patras requires characterising the expected lead times and student exposure and evaluating the different damage levels the archetype building could experience at various levels of ground-shaking intensity. The latter requirement can be accomplished using building-level seismic fragility relationships, which provide the probability of exceeding different building-level, structure-specific damage levels as a function of ground-shaking intensity. The procedure implemented to derive the fragility relationships for the archetype school building developed in Section 3 is further explained in the following sub-sections.

4.1. Damage-state definition

A structure could incur different damage conditions (levels) depending on its seismic performance characteristics and the ground-shaking intensity level. To describe these conditions, four different structure-specific, building-level damage states (DSs) are defined. The occurrence of each DS is quantified using an appropriate measurable engineering demand parameter (EDP). This study adopts the maximum interstorey drift ratio (MIDR) as an EDP, which is a highly reliable proxy to characterise global structural/nonstructural damage, particularly for drift-sensitive components (e.g., [50]). The MIDR threshold that corresponds to the occurrence of each DS is mapped by assessing multiple measurable damage criteria during pushover analysis. Similarly to [51], these criteria represent varying stages of seismic damage at different resolutions; e.g., section, component, and storey levels. The criteria used here are adopted from [52,53] and are also summarised in Table 2. The thresholds of different DSs are based on the first occurrence of any criterion in a given column of Table 2. Note that θ_y denotes the yield rotation and θ_u represents the ultimate rotation quantified as per Eurocode 8–3 [54].

Fig. 5 illustrates the pushover curves for both frames and the MIDR thresholds of each DS. The thresholds are also provided in Table 3, along with some relevant dynamic characteristics, i.e., the fundamental period of vibration (T_1) for both infilled and bare configurations, in addition to the mass participation ratio. The pushover analysis demonstrates a good distribution of inelastic deformation demands among the frames' two floors, with a slightly higher demand concentration on the first floor. Consequently, the mapped DS thresholds are governed by the damage observations recorded on the first floor rather than the second. Furthermore,

Table 1
Average mechanical properties of the modelled infill walls.

Parameter	Symbol	Units	Value
Compressive strength	σ_{m0}	MPa	6
Shear strength	τ_{m0}	MPa	0.4648
Modulus of elasticity	E_m	MPa	4312
Slide resistance	τ_0	MPa	0.3254
Vertical gravity stress	σ_0	MPa	0
Thickness of infills	t	mm	100

Fig. 5a shows that the longitudinal frame has slightly more lateral strength and stiffness than the transverse one, which means that the latter frame develops earlier infill cracking and yielding of structural elements, as also indicated by the MIDR thresholds of DS0 and DS1. The difference in characteristics associated with both directions is attributed to the distribution of infill walls. The longitudinal frame is fully infilled whereas the last bay of the transverse structure represents an external open corridor that does not incorporate any infill walls, leading to a slight reduction in the overall lateral strength and stiffness.

4.2. Seismic performance characterisation using dynamic analysis

To derive fragility relationships, the seismic performance of the developed archetype school models must first be characterised. We achieve this by conducting nonlinear dynamic response analyses following the multiple-stripe-analysis (MSA) approach (e.g., [55]). MSA involves subjecting the archetype school models to multiple sets of ground-motion records, each representing a discrete level of a pre-defined ground-shaking IM. The IM adopted in this study is the spectral acceleration at the structure's fundamental period (Sa (T_1)). We assume a T_1 value equal to 0.4s, representing the bare-frame configuration of the archetype school building in both longitudinal and transverse directions (see Table 4). We neglect the value of T_1 that corresponds to the infilled frames, given their susceptibility to early cracking, which leads to significant period elongation due to the loss of the structure's lateral stiffness (even under low ground-shaking levels).

The considered MSA approach involves adopting ground-motion records that are consistent with the seismic hazard of the site of interest. This, in turn, requires performing probabilistic seismic hazard analysis (PSHA) for Patras, followed by selecting hazard-consistent ground-motion record sets to be implemented in nonlinear analysis. These procedures produce unique sets of 20 hazard-consistent two-component ground-motion records at seven different IM values, which reflect varying levels of seismic hazard expressed in terms of their mean return period (T_R). The selected IM values represent hazard levels with T_R ranging from 30 to 4995 years. Further details on the PSHA conducted for Patras and the adopted record-selection procedure are found in Appendix B.

Fig. 6 illustrates the MSA results for the frames in the longitudinal and transverse directions. The vertical lines represent the MIDR thresholds for the different considered DSs (see Table 3). It can be observed that both frames perform well, even at high IM, i.e., Sa (T_1), levels, which is mainly due to the strict seismic design requirements imposed by Eurocode 8. This is further confirmed in Table 4, which indicates that both the longitudinal and transverse frames remain completely undamaged in 22% and 11% of analysis cases, respectively. Both frames experience low levels of damage (i.e., DS0 and DS1) in up to 65% of the analysis cases, whereas the high DSs, including DS2 and DS3, are experienced in less than 22% of cases.

4.3. Derivation of building-level fragility relationships

We use the MSA results to derive building-level fragility relationships, which define the probability of exceeding the different DSs that the archetype school models could incur over a range of IM levels. These relationships are determined by fitting lognormal cumulative distribution functions to the MSA results via the maximum likelihood approach suggested in [56]. The fragility relationships fit for both frames are shown in Fig. 7. The median (μ_{DSi}) and dispersion (β_{DSi}) of the relationships are also reported in Table 5. The μ_{DS2} and μ_{DS3} values for both frames are relatively similar. In contrast, the μ_{DS0} and μ_{DS1} values for the longitudinal frame are noticeably larger than those of the transverse frame. This is attributed to the former frame's higher lateral strength and stiffness, which leads to earlier development of both cracking of infill walls and yielding of structural elements in the transverse frame, as explained in Section 4.1. The previous observations indicate that the archetype building is more susceptible to slight and moderate damages at lower IM levels in the short direction than in the longitudinal direction. In contrast, the archetype building is expected to perform similarly in both orthogonal directions for high damage levels and near-collapse conditions.

5. EEW feasibility for school buildings in Patras

In this section, we investigate the potential implementation of EEW systems in the city of Patras by evaluating the EEW lead times (i.e., the available time to implement safety measures before the arrival of potentially damaging seismic waves at target sites of interest) for different station configurations, considering both regional and onsite EEW approaches. We then focus on the onsite EEW approach and use the potentially useful lead times, along with student exposure (i.e., number of students in each school) and expected damage (based on the archetype building and its fragility relationships defined in Sections 3-4), to identify schools for which the deployment of an EEW system could be more beneficial.

Table 2
Criteria for mapping MIDR thresholds to DS occurrences; adopted from[52,53].

Damage Level	Slight Damage DS0	Moderate Damage DS1	Extensive Damage DS2	Near Collapse DS3
Section Level	N.A.	Reaching yield bending in a supporting column	Reaching maximum bending strength of a column	Reaching shear failure in any element
Component Level	Majority of infills develop first crack	Reaching the value of θ_y in a supporting column	Reaching 75% of the θ_u in any component	Reaching the θ_u in any component
Global Level	N.A.	Reaching the global yield point of the structure of the structure	Reaching the maximum strength of the structure	About 20% drop in the maximum strength
General description of the DS	Nonstructural damage due to infill cracking only	Moderate structural and nonstructural damage with no significant yielding of members	Severe structural and nonstructural damage. Some retained residual strength and stiffness	Full exploitation of strength and ductility. Very low residual strength and stiffness

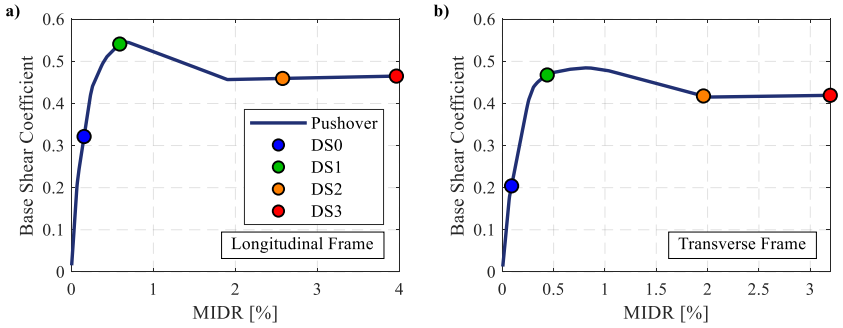

Fig. 5. Pushover curves and MIDR thresholds of the considered DSs for (a) Frame 3-3 in the longitudinal direction; and (b) Frame B–B in the short direction. Note that the base shear coefficient is the ratio between the structure's base shear and seismic weight.

Table 3
MIDR thresholds of the considered DSs and dynamic properties of the archetype school models.

Property	Frame direction	DS0	DS1	DS2	DS3
MIDR threshold [%]	Longitudinal direction	0.15	0.59	2.58	3.96
	Transverse direction	0.09	0.44	1.96	3.20
Fundamental period T_1 [s] – infilled frame	Longitudinal direction	0.13 (91.5% mass participation ratio)			
	Transverse direction	0.14 (92.3% mass participation ratio)			
Fundamental period T_1 [s] – bare frame	Longitudinal direction	0.39 (86.2% mass participation ratio)			
	Transverse direction	0.41 (84.9% mass participation ratio)			

Table 4
Number and proportion of analysis cases for each DS.

Frame	Undamaged	DS0	DS1	DS2	DS3
Longitudinal direction	62 (22%)	79 (28%)	82 (29%)	19 (7%)	38 (14%)
Transversal direction	33 (11%)	83 (29%)	101 (36%)	26 (9%)	37 (13%)

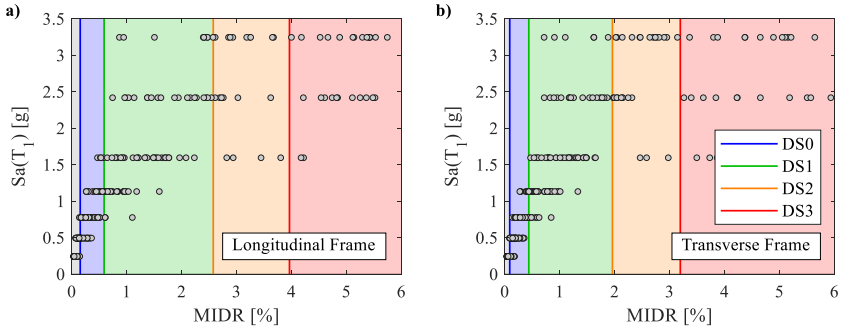

Fig. 6. MSA results for a) Frame 3-3 in the longitudinal direction; and b) Frame B–B in the short direction.

5.1. Lead-time and damage potential computations for Patras

We estimate the theoretical EEW lead time available for Patras (approximated by a point with coordinates 21.73457°N, 38.24664°E), for four EEW/station configuration scenarios. The first three scenarios consider a regional EEW system consisting of a network of seismic sensors located in or around potential epicentral areas, which detect/measure *P*-waves (or early portions of *S*-waves) close to a seismic rupture and send out alerts to target sites far away, ahead of the arrival of damaging *S*-waves. This regional EEW system consists of only TURNkey stations in the first scenario, for which EEW is facilitated through the connection of the TURNkey stations to the TURNkey FWCR platform. The second scenario incorporates all strong-motion stations in the region (i.e., those monitored by HUSN and the TURNkey stations) within the system. The third scenario includes all seismic stations in the region (not just strong-motion stations) within the system. These second and third scenarios are considered to assess the potential benefits of expanding the EEW system to the entire Patras region (i.e., to enable longer lead times). The fourth scenario considers an onsite EEW system, which typically consists of a limited set of/single seismic stations located at (for site-specific systems) or near (for front-detection systems) particular target sites/infrastructure of interest; in this case, the system comprises a single station located at the representative coordinates of Patras. This type of system estimates source parameters or, more often, ground-motion IMs directly, based on characteristics of the seismograms recorded within the system (e.g., [4]). In general, regional EEW systems yield more

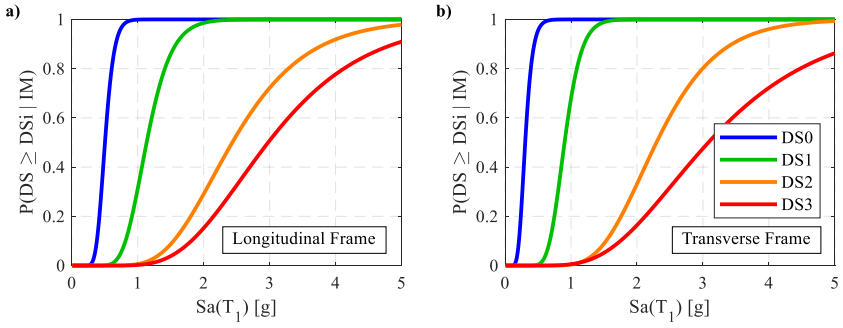

Fig. 7. Fragility functions for a) Frame 3-3 in the longitudinal direction; and b) Frame B–B in the short direction.

Table 5
Median and dispersion parameters of the fragility curves for the two frames.

DS/Parameter	Longitudinal Direction		Transverse Direction	
	μ_{DSi} [g]	β_{DSi}	μ_{DSi} [g]	β_{DSi}
DS0	0.503	0.219	0.305	0.291
DS1	1.135	0.258	0.902	0.222
DS2	2.433	0.355	2.295	0.316
DS3	2.977	0.387	3.082	0.442

accurate estimates of the source parameters, but onsite EEW systems result in faster warning times for near-source targets. Note that our feasibility analysis does not consider variations in the accuracy performance of different sensor types. This would require further extensive investigation, involving the application of specific algorithms for earthquake detection and source parameter characterisation to recorded data, for instance (e.g., [57,58]).

We perform different types of analyses to 1) identify the seismic sources associated with the longest lead times and greatest damage potential (i.e., deterministic analyses); and 2) evaluate lead-time distributions (i.e., probabilistic analyses). We compute lead times for both types of analyses using the source models developed in the framework of the *Seismic Hazard Harmonization in Europe* (SHARE) Project [59]. The fault model for the deterministic analyses is included in the Greek Database of Seismogenic Sources (GreDaSS; [21]), and the European Database of Seismogenic Faults (EDSF; [60]). We adopt the area source model of the 2013 European Seismic Hazard Model (ESHM13 model; [61]) for the probabilistic analyses. In both cases, we assume point sources located at the nodes of a $0.1^\circ \times 0.1^\circ$ resolution 2D grid, retaining only those within the individual seismogenic sources (i.e., faults) or the crustal area source model (as appropriate). Each point source is characterised by the parameters of the associated source model. In the case of faults (i.e., deterministic analyses), each source is defined by a single magnitude identified as the corresponding fault's maximum (moment) magnitude. The depth is defined as the minimum fault depth plus 2/3 of the fault's vertical width (i.e., the difference between the maximum and minimum fault depths), in line with the observation that ruptures tend to nucleate in the deeper sections of the fault [62]. The focal mechanism is defined based on the specific fault's average strike, dip, and rake values. In the case of area sources (i.e., probabilistic analyses), we generate a synthetic catalogue of 1000 earthquakes for each point source by assuming the Gutenberg-Richter (GR) distribution of the corresponding area source. The minimum magnitude is set as $M_w = 4.5$, and the maximum magnitude is computed as the weighted average of the four maximum magnitudes proposed for each area source. Each point source is also characterised by the weighted average depth value and the focal mechanism parameters (strike, dip, rake) associated with the highest weight.

We compute lead times only from sources capable of causing some damage. In particular, we consider the four structure-specific building-level DSs (i.e., slight, moderate, extensive, near collapse) defined in Section 4.1 and the corresponding building-level fragility relationships derived in Section 4.3 (Table 5) to define Sa (T_1) thresholds for each considered DS (Table 6). Thresholds are defined as the 5th-percentile values from the relevant lognormal fragility relationship, i.e., they correspond to Sa (T_1) values providing a 5% probability of exceedance for each DS.

We define the median ground shaking in Patras in terms of Sa ($T_1 = 0.4$ s) using a Ground Motion Model (GMM). The appropriate GMM is identified by evaluating the relative performance of various candidate GMMs against a common ground-motion dataset for the studied area [63]. This dataset contains 5790 PGA values recorded in the region of interest up to a maximum Joyner-Boore distance (R_{JB}) of 200 km from 273 shallow events (depth <30 km) with M_w ranging between 4 and 6.7. We adopt multiple scoring techniques to measure the performance of the models, namely the log-likelihood method [64] ; the pari-mutuel gambling score [65]; the quantile score [65]; the Euclidean metric distance [66]; and the Deviance Information Criterion [67]. Based on this analysis, the GMM with the best performance is that proposed in [65]. We use lognormal mean values increased by one standard deviation to compute the damage level, which is defined as the largest DS for which the threshold is exceeded at the computed Sa ($T_1 = 0.4$ s) value. We obtain R_{JB} estimates (required for the considered GMM) from epicentral distances, using the conversion coefficients proposed in [68] for the style-of-faulting and tectonic setting of the associated seismic source. We consider a representative value of V_{s30} (the average seismic shear-wave velocity from the surface to a depth of 30 m) equal to 350 m/s, which we define based on a V_{s30} map compiled in [69] by combining information from various sources [70,71]. Finally, we obtain lead times from the theoretical arrival times of *P*- and *S*-waves

in a 1D spherically symmetric velocity model computed using the *Obspy. taup* package that is based on the Java TauP Toolkit in [72]. This velocity model was prepared by replacing the shallow layers of the IASP91 model [73] with the context-specific velocity model in [74], with the *S*-wave velocities obtained from the Poisson solid's approximation. We calculate the lead times in Patras for a regional EEW configuration according to Eq. (1):

$$LT_{regional} = TT_a^S - TT_{a,st3}^P - \delta_m - \delta_t \quad (1)$$

where TT_a^S is the *S*-wave arrival time in Patras from source *a* and $TT_{i,st3}^P$ is the *P*-wave arrival time at the third closest station to source *a* (*st3*). δ_m represents the time required to compute the magnitude of the ongoing event and is assumed to be equal to 3 s for $M_w < 6.5$; 4 s for $6.5 \leq M_w < 7$; 12 s for $7 \leq M_w < 7.5$; and 20 s for $M_w \geq 7.5$ (e.g., [75]). δ_t captures data telemetry delays, which are idealistically assumed to comprise 1 s for data transmission and 1 s for issuing the warning message (e.g., [76,77]). We calculate the lead times in Patras for an onsite EEW configuration through Eq. (2):

$$LT_{on-site} = TT_a^S - TT_a^P - 3 \quad (2)$$

where TT_a^P is the *P*-wave arrival time in Patras from a source *a,* and 3s accounts for processing time (e.g., [78,79]). The lead times are computed based on the theoretical arrival time of the *S*-wave. In most cases, the peak value of ground shaking is generally expected to occur at a later time (either on the *S*-waves or on surface waves), thus providing additional warning time with respect to those computed in this study. Note that lead-time computations are performed according to Eqs. (1) and (2), without considering uncertainties inherent in the underlying parameters. (For instance, uncertainties in the delay times would relate to the number of sensors required to locate the event and estimate its magnitude, the algorithms selected for signal acquisition and EEW processing, and technological components, such as sensor/datalogger and communication systems). Thus, the analyses presented in this study must be considered a first-level feasibility study that evaluate the effects of different EEW configurations (in terms of density and geometry of the seismic network) on the computed lead times under nominal conditions.

Results from the deterministic analyses are provided in Fig. 8, which can be used to identify seismic sources responsible for the longest lead times and greatest damage potential. In the case of a regional EEW system based on the TURNkey network only (Fig. 8a), the maximum lead time is 7s, which is associated with the sources located in the Western Corinth Gulf area. The blind zone (i.e., the area too close to the source region, where no alert is possible) is not isotropic due to the non-homogenous distribution of the low-cost strong-motion TURNkey sensors (the presence of the blind zone depends on source-to-site distances, station density and layout, the number of stations required to issue an alert , and technical time requirements, e.g., processing times and telemetry delays). The blind zone is especially extended in the west-southwest direction because the considered sensors are located in the proximity of the city of Patras (Fig. 1). This analysis highlights some limitations of the TURNkey seismic sensor network in terms of EEW regional system potential, especially if compared with an ideal regional EEW system based on all the strong-motion stations in the region (including the TURNkey stations) (Fig. 8b). Both network configurations perform similarly for the seismic sources located in the Western Corinth Gulf area, but the regional EEW system that accounts for all strong-motion stations is characterised by a reduced blind zone (i.e., two seismic sources instead of six producing no warning) and longer lead times (up to 14s). This is due to the rapid detection of strong offshore events by non-TURNkey stations located in the Ionian Islands. The results of the lead-time and damage potential analysis for the third regional EEW scenario - also considering broadband and short-period sensors (which usually saturate in the proximity of the source), assuming that these stations could and may be equipped with collocated strong-motion sensors in the future (where needed) - are shown in Fig. 8c, and exhibit slightly higher lead times, up to 16s. Fig. 8d illustrates the lead times associated with the onsite EEW configuration; this map is characterised by no blind zone. However, the lead times for the closest sources of the Western Corinth Gulf area are shorter than those obtained for the regional EEW configurations. The lead times associated with the Ionian Islands seismic sources (maximum value of about 12s) are between those that result from the regional EEW configuration based on the TURNkey network only and those that are obtained for the regional EEW configuration based on all strong-motion sensors in the studied area.

The most common damage level across the four considered station configurations is *slight*, and most *near collapse* damage occurs in the blind zone. *Moderate* damage levels are associated with minimal available lead time (up to 2.5 s), which means that the EEW system can only be helpful for these cases if coupled with very rapid mitigation actions (i.e., automatic shutdown of specific school lab equipment). In contrast, the larger lead times associated with *slight* damage could allow the students to take refuge under the desks, find a safe place in the same/adjacent room, or even evacuate the school's ground floors.

The deterministic analyses only estimate the lead times and damage potential associated with maximum magnitude earthquakes on known faults. In contrast, the probabilistic analyses consider the recurrence of 3849 GR-distributed synthetic seismic events capable of producing damage in Patras, to evaluate the lead-time probability distribution for the given target site. Histograms representing the distribution of lead times associated with the four seismic network configurations are provided in Fig. 9. Note that negative lead times

Table 6
IM thresholds associated with each considered DS for the archetype school building.

Damage state (DS)	Sa (T_1 = 0.4 s) threshold (g)
Slight (DS0)	0.19
Moderate (DS1)	0.63
Extensive (DS2)	1.36
Near Collapse (DS3)	1.49

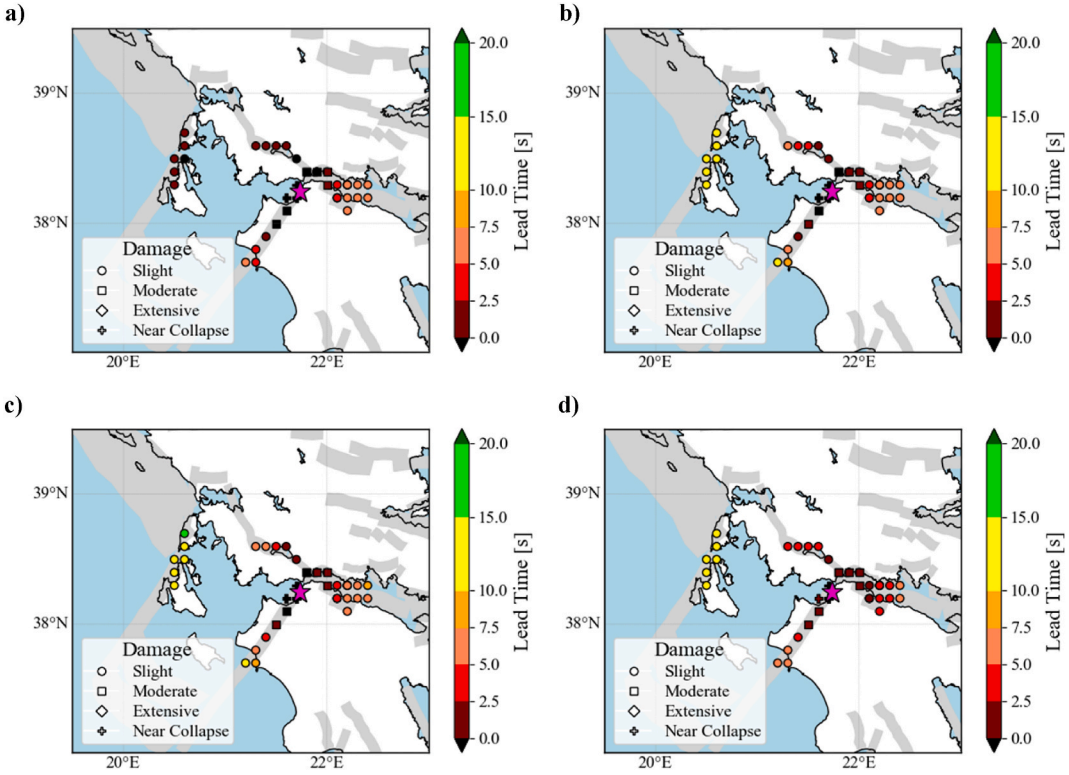

Fig. 8. Deterministic lead time and damage potential maps for Patras associated with a) a regional EEW configuration based on the TURNkey stations only; b) a regional EEW configuration based on all the strong-motion stations in the region; c) a regional EEW configuration based on all the seismic stations in the region; d) an onsite EEW configuration. Coloured symbols identify the seismic sources responsible for a specific lead time/damage level in Patras (magenta star). The colours represent the lead times, while the symbols denote the damage. Gray-shaded areas represent the EDSF [60] fault model.

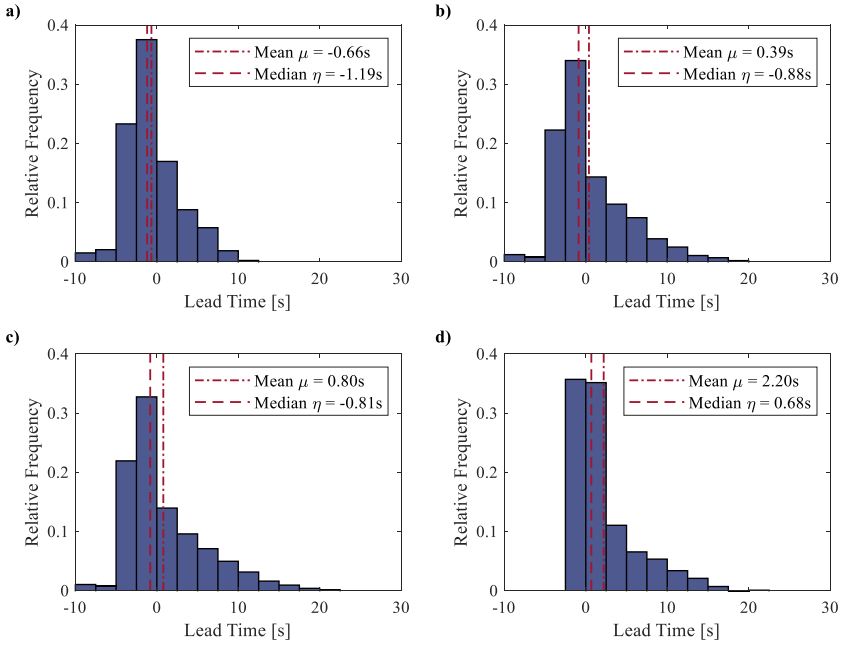

Fig. 9. Probabilistic lead times for Patras associated with a) a regional EEW configuration based on the TURNkey stations only; b) a regional EEW configuration based on all the strong-motion stations in the region; c) a regional EEW configuration based on all the seismic stations in the region; d) an onsite EEW configuration.

correspond to blind zones.

Despite differences in the underlying source models, maximum lead times obtained from the probabilistic analyses align with those provided in Fig. 8. In particular, the shortest mean lead time is associated with the regional EEW configuration based on the TURNkey stations only, while the longest mean lead time is associated with the regional EEW configuration based on all the seismic stations in the region. Most lead times are negative for the regional EEW configurations, which is reflected in their median values. Positive median lead time ($\eta = 0.68$s) and the highest mean lead time ($\mu = 2.2$s) are obtained for the onsite EEW configuration, resulting from its narrower blind zone.

Fig. 10 shows the earthquake contributions to the computed lead times for the onsite EEW configuration, both in terms of M_w (Fig. 10a) and R_{JB} (Fig. 10b), recalling that only earthquakes capable of causing damage are considered for computing lead times. The figures highlight that lead times near the computed median are associated with earthquakes of approximately 5.5 magnitude that mostly occur at very short distances (less than 15 km). In contrast, larger magnitudes (up to 7.5) produce less frequent long lead times at farther distances (up to 120 km), which correspond with the strong seismic sources near the Ionian Islands. Fig. 10c also provides the damage level as a function of the computed lead times, indicating that the dominant damage level is slight at all lead-time values. More severe damage is associated with shorter lead times, as observed before.

The results of both types of analyses suggest that the EEW for Patras is feasible and that the regional EEW system being deployed for the TURNkey project could benefit from integration not only with the existing sensors in the region but also from integration with an onsite EEW system. An integrated regional/onsite earthquake early warning system for Greece has also been recently proposed in [80].

5.2. EEW relative feasibility index for schools

We now investigate EEW feasibility for the 268 schools identified in the case-study region to determine schools that would most benefit from an onsite EEW system. Specifically, we characterise each school through an EEW relative feasibility index (*RF*). The *RF* metric was first proposed in [9] and is refined/tailored here for the specific application of interest. The modified *RF* metric leveraged in this study combines estimates of lead time (*L*), damage state (*DS*), and the number of exposed students (*S*) into a single indicator:

$$RF_j = F_L(L_j) \times w_L + F_{DS}(DS_j) \times w_D + F_S(S_j) \times w_S \quad (3)$$

where j represents the considered target site (i.e., a school building in this case), $F_X(X_j)$ is the empirical cumulative distribution function of X (across all examined schools) evaluated at j, and w_X is the weight for X (such that $w_L + w_D + w_S = 1$). Each $F_X(X_j)$ function ranks the schools based on the underlying metric (i.e., *L*, *DS,* or *S*). The weights are user-defined and can account for stakeholder priorities towards each feasibility feature. The maximum theoretical value of RF_j is 1, achieved if the school j is simultaneously associated with the longest lead time, the greatest damage, and the highest number of students.

We compute lead time and damage estimates from a probabilistic analysis associated with an on-site EEW configuration similar to that described in the previous section. The main difference is that the analysis performed here considers the exact location of each school with an accurate estimate of V_{s30} at the school site [69]. Moreover, we limit our analysis to lead times capable of facilitating some mitigation actions (such as the shutting down of computers or DCHO) by only considering events capable of causing damage (slight or higher) with $M_w \geq 6.5$ and $R_{JB} \geq 50$ km (which allow lead times > 5s according to Fig. 10). We, therefore, obtain probabilistic lead-time/damage distributions at the 268 school locations, from which we evaluate the median lead time and median damage state (according to the DS thresholds defined and the point on the Sa(T1) distribution used in the previous section) that we use as lead time and damage proxies, respectively, in Eq. (3). Given the adopted magnitude/distance constraint, the median lead times at the school locations range from 8.5s to 10s, and the median damage state is slight for all schools. We use the number of students for the school year 2018–2019.[9] To correct for discrepancies in the length of the school day across different schools (i.e., about 6 h or 9 h) and ensure a fair comparison in terms of school occupancy, the number of students in 6-h-day schools is scaled by a factor of 2/3. The corrected number of students ranges from 2 to 503.

RF indices for an equally-weighted case ($w_L = w_D = w_S = 0.333$) are provided in Fig. 11. Higher values indicate schools that should be prioritised for the deployment of onsite EEW systems. They correspond to schools with relatively long lead times and a large corrected number of students (all characterised by slight damage). The schools with the highest (0.64) and lowest (0.02) feasibility index, respectively, are shown in Table 7; the school with the highest corrected number of students (503) ranks second (with a lead time of 9.66s), while the school with the longest lead time (10s) ranks 75th, due to its low corrected number of students (28). The proposed EEW *RF* Index does not account for warning accuracy, which would involve additional detailed analyses of specific algorithms in operational EEW platforms outside the scope of the study. Examination of warning accuracy was previously carried out for selected testbed sites across Europe by some of the authors (e.g., [57,58]).

6. Demonstrating a risk-informed EEW decision-support system for the archetype school

The establishment of a risk-informed EEW decision-support system for the developed archetype school building requires building-specific losses (consequences) to be quantified. Seismic losses are evaluated here using the component-based methodology introduced in the FEMA P-58 guidelines [50]. This procedure quantifies the total loss (e.g., repair cost, repair time, casualties) in a building by aggregating the losses sustained by its individual structural and nonstructural components. The FEMA P-58 methodology integrates

[9] https://data.gov.gr.

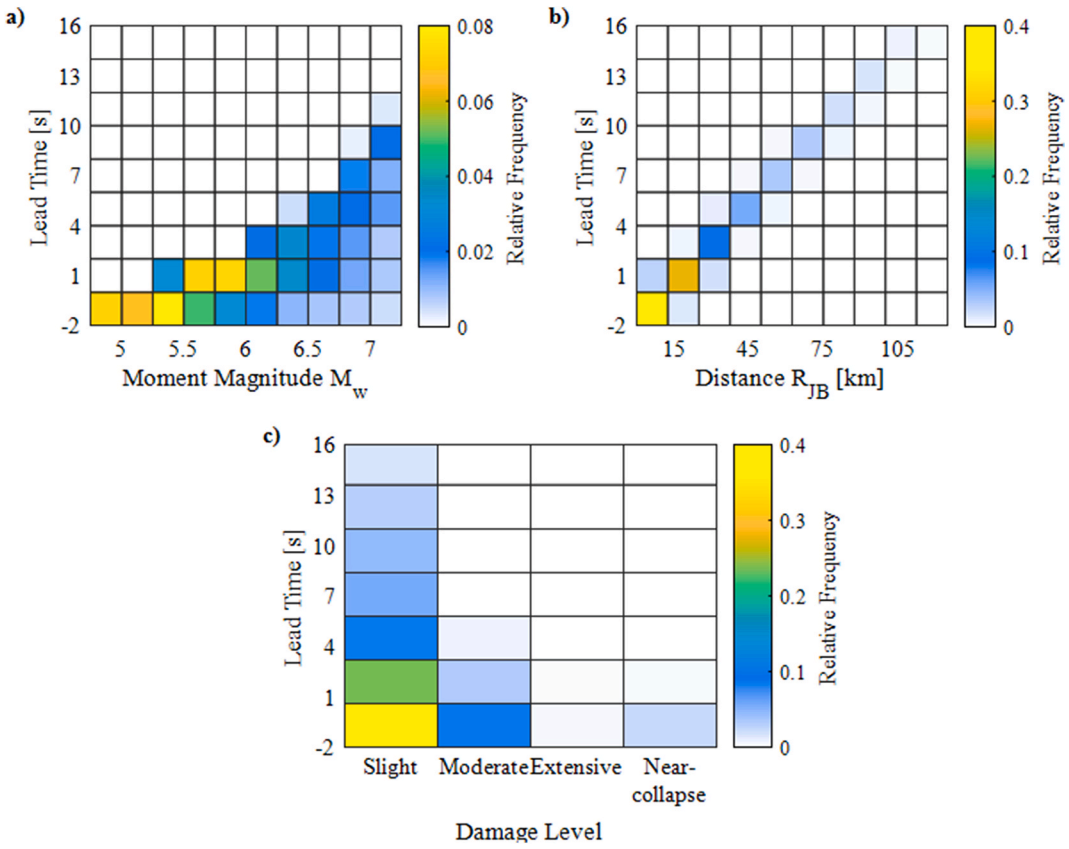

Fig. 10. Probabilistic lead times for Patras associated with an onsite EEW configuration, expressed as a function of (a) moment magnitude M_w; (b) Joyner-Boore distance R_{JB}; and (c) damage level.

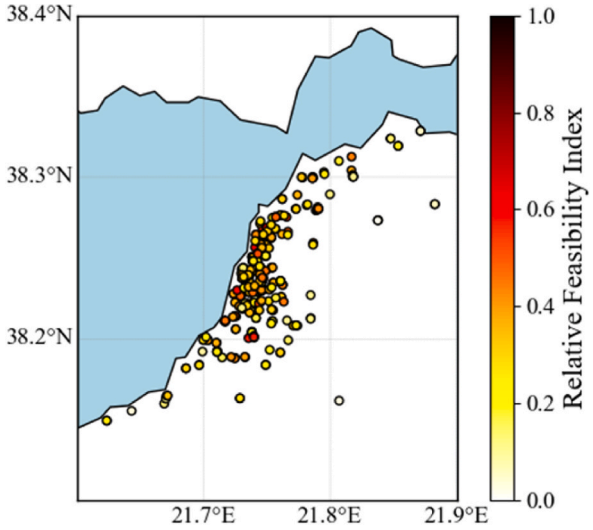

Fig. 11. EEW Relative Feasibility Index at the school locations for an equally-weighted case (i.e., $w_L = w_D = w_S = 0.333$).

four phases: seismic hazard characterisation, structural response analysis, damage evaluation, and loss assessment. The seismic hazard of Patras is assessed by conducting PSHA (see Appendix B for details). Furthermore, the nonlinear response of the archetype school models is characterised by MSA, as explained in Section 4.2. The FEMA P-58 methodology additionally requires the definition of a comprehensive inventory of structural and nonstructural components, together with their fragility and consequence models that are used to quantify the damage and loss incurred by each building component when the archetype building is subjected to ground

Table 7
Schools in Greece with the highest and lowest EEW Relative Feasibility Index, respectively, for an equally-weighted case (i.e., $w_L = w_D = w_S = 0.333$).

Rank	School	Longitude	Latitude	V_{s30} [m/s]	Median Lead Time [s]	Median Damage	Corrected Number of Students	Relative Feasibility Index
1	1 & 6 Junior High School	21.74068	38.25664	220.249	9.749727	Slight	257	0.64
268	Kindergarten Of Ano Kastritsi	21.83753	38.27333	589.00	8.706967	Slight	9	0.02

shaking. In this study, the compilation of the component inventory and estimation of seismic losses following the FEMA P-58 methodology are carried out using the seismic performance prediction (SP3[10]) software. Further details are provided in subsequent sections.

6.1. Inventory of damageable structural and nonstructural components

Each structural and nonstructural component is associated with a specific component-level fragility model expressed in terms of an appropriate EDP, e.g., interstorey drift ratio (IDR) or peak floor acceleration (PFA). A component-level consequence function then converts the damage into losses (e.g., repair costs, repair time, or casualties).

The component types/categories used for the archetype school building in this study are similar to those defined in [81] which developed a component inventory from in-situ surveys of school buildings in Italy. This inventory is also deemed appropriate for Greek school buildings due to the similarities in construction practices across countries in the Mediterranean region and because, Greece-specific fragility and consequence models are not available in the literature for the selected components (to the best of the authors' knowledge). Similarly to [81], we implement the default fragility and consequence models provided by SP3 software where alternatives are not available. The simplified approach introduced in [82] is adopted to convert USA-based repair-cost consequences to the European context, considering the appropriate differences in construction and labour costs. In addition, the effects of currency inflation are accounted for per the default approach of SP3.

Masonry infill walls are explicitly included in the analysis, given their potentially significant contribution to seismic losses, especially under low-to-moderate seismic shaking (e.g., [44,45]). These components are not part of the default SP3 component library, so we use the fragility and consequence models for masonry infill walls proposed in [45]. These consequence models include average repair costs only that we combine with the dispersion coefficients proposed in [83]. Although the adopted fragility model from [45] was calibrated based on experimental data from the general Mediterranean region, the corresponding consequence models are based on repair costs and operations applicable to Italy. This issue is accounted for by converting the repair costs to Greece-based estimates using the approach proposed in [82]. The final inventory of components is reported in Table 8, together with the required EDPs and the corresponding references for fragility/consequence models.

6.2. Component-based loss estimation

We perform the seismic loss calculation through SP3, inputting both seismic hazard information and response-analysis (MSA) results. The SP3 default values for replacement cost, replacement time, and ASCE 7–10 [109] Risk Category are adopted for the archetype school building. These values are respectively equal to \$296/ft^2 (\$3186/m^2), 169 days per storey, and III. The default building-repair fragility in SP3 is also adopted to account for the possibility that the structure becomes irreparable due to excessive residual drifts. The structural collapse potential at different IMs is addressed by assigning a collapse fragility relationship in SP3, which is conservatively assumed equal to the DS3 fragility relationship (near collapse; Table 5).

Fig. 12a depicts the mean repair-cost ratio for the archetype school building at different hazard levels, expressed in terms of the mean return period (T_R). The mean repair-cost ratios are expectedly low (<10%) up to the hazard level defined by a T_R of 475-years; this observation can be attributed to the strict seismic design provisions imposed by Eurocode 8. At larger hazard levels ($T_R \geq 975$ years), the mean repair-cost ratio is at least 43% and reaches almost 100% at a T_R equal to 4995 years. The expected annual loss is computed as 0.17%. Fig. 12b reports the relative contribution of different component types (and structural behaviours) to the mean seismic repair costs, i.e., structural and nonstructural components, collapse occurrences, and demolitions due to large residual drifts. As expected, the primary contributor to the repair costs at hazard levels with $T_R \leq 225$ years is the nonstructural components (and the masonry infill walls in particular). For $T_R > 475$ years, the relative contribution of the nonstructural components becomes the smallest, and the losses are dominated by the collapse and demolition cases. Similar observations can also be found in other studies (e.g., [81,84,85]).

Fig. 13a illustrates the mean repair-time ratio, which represents the time needed to accomplish repair activities normalised by the total replacement time. It can be observed that the mean repair-time ratios at T_R values less than 475 years are considerably higher than the repair-cost ratios (see Fig. 12a). The mean-repair time ratios become significantly large (at least 68%) at $T_R \geq 975$ years until reaching 100% at a T_R equal to 4995 years. Fig. 13b reports the mean casualties at each T_R. The number of casualties is almost close to zero at T_R levels less than 975 years. This is attributed to the fact that structural collapse, which constitutes the primary cause of casualties, is unlikely to occur at such hazard levels. Conversely, the mean number of casualties start to increase rapidly from 1 at a T_R value of 975 years to 8 at T_R equal to 4995 years.

[10] https://www.sp3risk.com.

Table 8
Inventory of all the damageable structural and nonstructural components used.

Fragility ID	Description of the functions	EDP	Unit	Reference
B1041.001a	ACI 318 SMF - Beam one side 24″ × 24″	IDR [%]	each	SP3 default as per FEMA P-58
B1041.001 b	ACI 318 SMF - Beam both side 24″ × 24″	IDR [%]	each	SP3 default as per FEMA P-58
N.A.	Masonry Infill Walls and Partitions - Clay	IDR [%]	m^2	[45]
C3032.003a	Suspended Ceiling for A<250 sf	PFA [g]	250 ft^2	SP3 default as per FEMA P-58
C3032.003 b	Suspended Ceiling for 250 < A<1000 sf	PFA [g]	250 ft^2	SP3 default as per FEMA P-58
C3032.003c	Suspended Ceiling for 1000 < A<2500 sf	PFA [g]	250 ft^2	SP3 default as per FEMA P-58
C3032.003 d	Suspended Ceiling for A>2500 sf	PFA [g]	250 ft^2	SP3 default as per FEMA P-58
C3034.002	Independent Pendant Lighting	PFA [g]	Each	SP3 default as per FEMA P-58
D2021.013a	Potable Water Piping	PFA [g]	1000 ft	SP3 default as per FEMA P-58
D2021.013 b	Potable Water Piping Bracing	PFA [g]	1000 ft	SP3 default as per FEMA P-58
D2021.023a	Potable Water Piping	PFA [g]	1000 ft	SP3 default as per FEMA P-58
D2021.023 b	Potable Water Piping Bracing	PFA [g]	1000 ft	SP3 default as per FEMA P-58
D2022.013a	Heating Water Piping	PFA [g]	1000 ft	SP3 default as per FEMA P-58
D2022.013 b	Heating Water Piping Bracing	PFA [g]	1000 ft	SP3 default as per FEMA P-58
D2022.023a	Heating Water Piping	PFA [g]	1000 ft	SP3 default as per FEMA P-58
D2022.023 b	Heating Water Piping Bracing	PFA [g]	1000 ft	SP3 default as per FEMA P-58
D2031.023a	Sanitary Water Piping	PFA [g]	1000 ft	SP3 default as per FEMA P-58
D2031.023 b	Sanitary Water Piping Bracing	PFA [g]	1000 ft	SP3 default as per FEMA P-58
D2061.023a	Steam Piping	PFA [g]	1000 ft	SP3 default as per FEMA P-58
D2061.023 b	Steam Piping	PFA [g]	1000 ft	SP3 default as per FEMA P-58
D3041.011c	HVAC Ducting	PFA [g]	1000 ft	SP3 default as per FEMA P-58
C2011.011a	Concrete Stairs with Seismic Joints	IDR [%]	each	SP3 default as per FEMA P-58
E2022.023	Desktop Electronics	PFA [g]	each	Fragility: SP3 default as per FEMA P-58; Consequence: $1000 repair cost & 1 day repair time (assume no uncertainty)

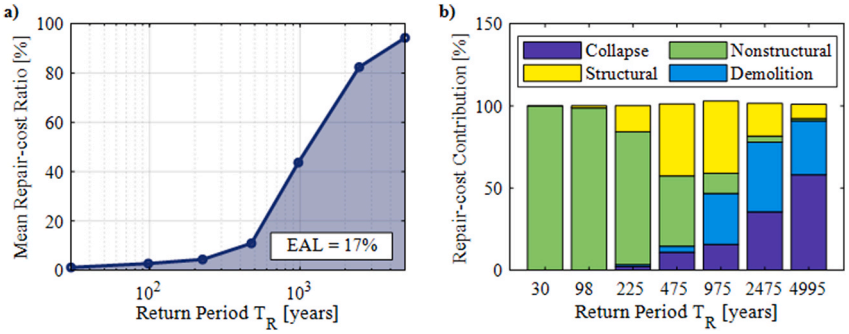

Fig. 12. Loss curves for: (a) mean repair-cost ratio; and b) relative contribution of different components to mean repair costs.

6.3. *Risk-informed EEW decision-support system for the archetype school*

We finally propose a risk-informed EEW decision-support system (DSS) for the schools in Patras, leveraging the methodology proposed in [8]. The DSS is designed to solve a binary decision-making problem (i.e., "trigger an EEW alarm" or "don't trigger an EEW alarm") for a given incoming ground motion based on the different types of consequences quantified in Section 6.2. We use a hypothetical EEW algorithm that can accurately estimate the final ground-shaking amplitudes (i.e., Sa (T_1) values) produced by an earthquake at the school with full certainty (although a more comprehensive decision-making approach that accounts for realistic

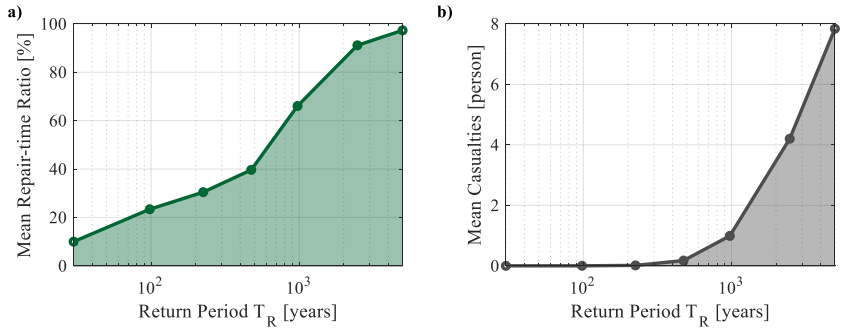

Fig. 13. Loss curves for: (a) mean repair-time ratio; and (b) mean casualties.

algorithmic uncertainties would also be possible if a suitable algorithm could be determined; see [8]). Then, the consequences of not triggering an EEW alarm (herein denoted as action $\overline{A}$) can be computed from:

$$E^{\overline{A}}\left(C_j^{\overline{A}}\middle|\mathrm{Sa}(T_1)\right)=\int_{c_j^{\overline{A}}}\int_{\mathbf{ds}} c_j^{\overline{A}} f^{\overline{A}}\left(C_j^{\overline{A}}\middle|\mathbf{ds}\right) f(\mathbf{ds}|\mathrm{Sa}(T_1))\, dc_j^{\overline{A}}\, d\mathbf{ds} \tag{4}$$

where $E^{\overline{A}}(C_j^{\overline{A}}\middle|\mathrm{Sa}(T_1))$ is the conditional expected value of the j-th type of consequence quantified in Section 6.2, $f(y|z)$ is the probability density function of y conditional on z, and **ds** is a vector version of damage states defined previously. $E^{\overline{A}}(C_j^{\overline{A}}\middle|\mathrm{Sa}(T_1))$ is computed using the results of the component-based seismic loss analysis in Section 6.2, such that $f(\mathbf{ds}|\mathrm{Sa}(T_1))=\int_{\mathbf{edp}} f(\mathbf{ds}|\mathbf{edp}) f(\mathbf{edp}|\mathrm{Sa}(T_1))\, d\mathbf{edp}$, and $f(\mathbf{ds}|\mathbf{edp})$ represents the appropriate component-level fragility functions.

For a given incoming amplitude of Sa (T_1), we assume that triggering an EEW alarm (herein denoted as action A_1) will eliminate from $E^{\overline{A}}(C_j^{\overline{A}}\middle|\mathrm{Sa}(T_1))$: (1) any casualties that are not caused by the building collapsing; and (2) any consequences associated with damage to laptops. In line with [8], a false alarm is assumed to occur if an incoming event does not cause damage to any component of the building, incurring a downtime (due to student panic and unrest) of 0.05 days and a needless inspection for building damage of $200. Finally, we assume that triggering an alarm incurs a flat reset fee of $600 (regardless of whether there is damage or not). The consequences for each action are summarised in the consequence matrix provided in Table 9.

The decision-making methodology requires the values of the consequence matrix to be normalised and weighted in line with stakeholder preferences towards the different types of losses considered. This can be obtained for A_1 and the jth type of loss according to Eq. (5):

$$r_{A_1,C_j}=\frac{E^{A_1}\left(C_j^{A_1}\middle|\mathrm{Sa}(T_1)\right)}{\sqrt{E^{A_1}\left(C_j^{A_1}\middle|\mathrm{Sa}(T_1)\right)^2+E^{\overline{A}}\left(C_j^{\overline{A}}\middle|\mathrm{Sa}(T_1)\right)^2}}w_j \tag{5}$$

where w_j represents the importance that the stakeholder places on mitigating $E^{A_1}(C_j^{A_1}\middle|\mathrm{Sa}(T_1))$. We specifically investigate the following sets of $\{w_j\}$ for this demonstration: (1) $w_1=w_2=w_3=0.333$ (i.e., a stakeholder has an equal preference for all criteria); (2) $w_1=0.90$ and $w_2=w_3=0.05$ (i.e., a stakeholder has a higher preference for mitigating direct cost); (3) $w_2=0.90$ and $w_1=w_3=0.05$ (i.e., a stakeholder has a higher preference for mitigating downtime); and (4) $w_3=0.90$ and $w_1=w_2=0.05$ (i.e., a stakeholder has a higher preference for mitigating casualties).

The final step in the methodology determines the optimal action for $\mathrm{Sa}(T_1)$ by first identifying the best and worst values for each type of loss across both options. The best option (v_j^+) for the j-th criterion is the one that minimises its value, i.e., $v_j^+=\min_j(r_{A_1,C_j}w_j, r_{\overline{A},C_j}w_j)$ and the worst value (v_j^-) is the alternative, i.e., $v_j^-=\max_j(r_{A_1,C_j}w_j, r_{\overline{A},C_j}w_j)$. The total distance of A_1 from the best (y_1^+) and worst (y_1^-) solutions are calculated from Eqs. (6) and (7), respectively:

$$y_1^+=\sqrt{\sum_{j=1}^{3}\left(v_j^+-\left(r_{A_1,C_j}w_j\right)\right)^2} \tag{6}$$

$$y_1^-=\sqrt{\sum_{j=1}^{3}\left(v_j^--\left(r_{A_1,C_j}w_j\right)\right)^2} \tag{7}$$

The optimal action (decision) is then the one with the largest S_i value, calculated according to Eq. (8):

$$S_i=\frac{y_i^-}{y_i^++y_i^-} \tag{8}$$

We determine the optimal decision for a range of Sa (T_1) values that could occur at the school building in future seismic events. The resulting EEW risk-informed DSS is provided in Fig. 14. It can be seen that the optimal action for a given Sa (T_1) can depend on stakeholder loss preferences; this finding is in line with previous applications of the decision-making methodology (e.g., [8,110]). The alarm is triggered at approximately Sa (T_1) = 0.15 g (around once every 13 years) for three of the weighting strategies considered but is only triggered at approximately Sa (T_1) = 0.20 g (about once every 21 years) if a stakeholder prioritizes the mitigation of financial (direct cost) losses. This higher EEW threshold is due to the flat reset fee associated with issuing the alarm, which is sufficient to counteract the benefits of mitigated EEW losses at lower ground shaking values. The variation in alarm threshold obtained for different stakeholder loss preferences underlines the importance of stakeholder engagement in the EEW decision-making process.

7. Conclusions

This paper adopted a risk-based approach to (1) investigate EEW feasibility for schools in Patras, Greece; and (2) demonstrate an engineering-oriented EEW decision support system for an archetype school building in the region. The study was motivated by EEW's promising potential to help mitigate some of the devastating effects of earthquakes (e.g., deaths, casualties, business interruption) - particularly in educational facilities - in the face of increasing exposure and vulnerability to seismic events worldwide.

First, an archetype school building was developed after conducting a remote survey of schools in Patras to determine the prevailing

Table 9
Consequence matrix for the EEW-DSS demonstration expressed as a function of Sa (T_1). $\alpha_{13}(\mathrm{Sa}(T_1))$ accounts for collapse-related casualties. Both $\alpha_{11}(\mathrm{Sa}(T_1))$ and $\alpha_{12}(\mathrm{Sa}(T_1))$ account for collapse-related laptop breakages. $p(FA|\mathrm{Sa}(T_1))$ denotes the probability of a false alarm. The 200, 0.05, and 600 values correspond to the alarm assumptions outlined in the text.

Action	C_1, direct cost ($)	C_2, downtime (days)	C_3, casualties (number)
A_1	$200p(FA\|\mathrm{Sa}(T_1)) + \alpha_{11}(\mathrm{Sa(T1)})E^{\overline{A}}(C_1{}^{\overline{A}}\|\mathrm{Sa}(T_1)) + 600$	$0.05p(FA\|\mathrm{Sa}(T_1))+E^{\overline{A}}(C_2{}^{\overline{A}}\|\mathrm{Sa}(T_1))\alpha_{12}(\mathrm{Sa}(T_1))$	$E^{\overline{A}}(C_3{}^{\overline{A}}\|\mathrm{Sa}(T_1))\alpha_{13}(\mathrm{Sa}(T_1))$
$\overline{A}$ (no action)	$E^{\overline{A}}(C_1{}^{\overline{A}}\|\mathrm{Sa}(T_1))$	$E^{\overline{A}}(C_2{}^{\overline{A}}\|\mathrm{Sa}(T_1))$	$E^{\overline{A}}(C_3{}^{\overline{A}}\|\mathrm{Sa}(T_1))$

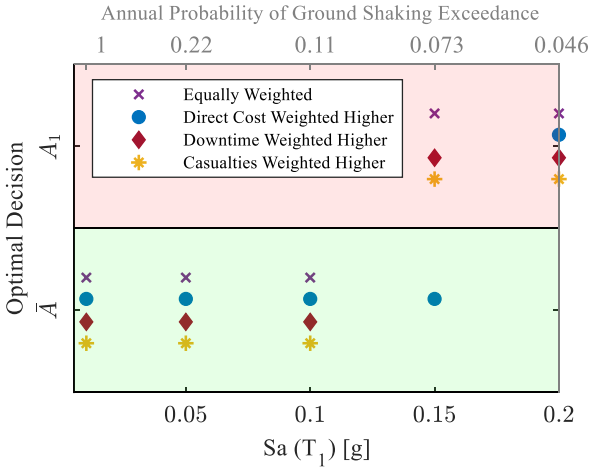

Fig. 14. Identifying the optimal EEW decision in terms of Sa (T_1). Note that A_1 is the action of triggering the EEW alarm and $\overline{A}$ means that no action is taken.

geometric features. Next, building-level fragility analysis was performed to assess the probability of exceeding different structure-specific damage states. This analysis showed that the archetype school building would likely experience low damage levels, even at high ground-shaking intensity, which is attributed to the strict seismic design provisions. The results of the fragility analysis were then adopted to investigate the potential usefulness of EEW lead times for schools in Patras with both deterministic and probabilistic analyses. In particular, the resulting lead-time estimates suggest that the regional EEW system deployed for the TURNkey project could benefit from integration not only with the sensors that already exist in the region but also from the integration with an onsite EEW system, thus enhancing the usefulness and reliability of the system. Our mapped feasibility results, which account for lead time, student exposure, and potential school damage, can be used to identify schools where an onsite EEW system could be most beneficial. For instance, the school with the highest feasibility index had a median lead time of approx. 9.74s, was characterised by slight damage and had 257 students (corrected). The school with the highest (corrected) number of students (503) ranked second (with a lead time of 9.66s and slight damage), while the school with the longest lead time (10s) ranked 75th due to its low corrected number of students (28).

The risk-informed EEW decision support system applied to the archetype school building represents a state-of-the-art engineering-oriented EEW approach. The system uniquely unifies state-of-practice earthquake engineering tools and multi-criteria decision-making techniques for informed stakeholder-driven EEW decision-making. Our application of the system considered traditional performance metrics used in PBEE (i.e., repair cost, repair time, and casualties), which were evaluated at the component level using the simulation-based FEMA P-58 risk assessment methodology. The risk-informed EEW decision support system additionally addressed a range of stakeholder preferences toward the metrics, demonstrating that the optimal risk-management action for a given level of impending shaking could depend on stakeholder priorities. For example (based on entirely assumptive data), it was found that the school's EEW system would trigger at a site in Patras approximately once every 13 years if stakeholders placed higher importance on limiting casualties or downtime. In contrast, it would only trigger approximately 60% as frequently if stakeholders prioritised mitigating direct cost. This finding emphasises the importance of considering end-user preferences in short-term earthquake risk management, which should be accounted for in ongoing installations of EEW in the region.

The results of this study contribute to the ongoing implementation of EEW in the Patras region as part of the TURNkey project and similar initiatives, identifying educational assets that should be prioritised for more detailed EEW feasibility investigations/investments in EEW implementation. The analyses also represent a first attempt to comprehensively quantify potential EEW effectiveness for schools through a rigorous risk-driven and engineering-oriented approach.

Credit Author statement

CG, EZ, and GC contributed to the study conception and design. Data collection was performed by KA and NM. Analysis was performed by CG, EZ, KA, and GC. The first draft of the manuscript was written by CG and EZ, and all authors commented on previous

versions of the manuscript. All authors read, revised, and approved the final manuscript.

Ethical approval

Ethics approval was not required for this study.

Funding details

This research was funded by the European Union's Horizon 2020 research and innovation program, specifically Grant Agreement Number 821046: TURNkey "Towards more Earthquake-resilient Urban Societies through a Multi-sensor-based Information System enabling Earthquake Forecasting, Early Warning and Rapid Response actions."

Informed consent

The research did not involve human participants and/or animals.

Declaration of competing interest

The authors declare that they have no known competing financial interests or personal relationships that could have appeared to influence the work reported in this paper.

Data availability

Data will be made available on request.

Acknowledgments

This research is funded by the European Union's Horizon 2020 research and innovation program, specifically Grant Agreement Number 821046: TURNkey "Towards more Earthquake-resilient Urban Societies through a Multi-sensor-based Information System enabling Earthquake Forecasting, Early Warning and Rapid Response actions." We thank Shunyao Cai and Daniel Alejandro Chavarria Gutierrez for supporting the remote data collection and the ground-motion record selection described in this study as part of their MSc Research Projects at UCL and IUSS Pavia respectively. We thank Dr Vincenzo Covertito (Vesuvius Observatory, National Institute of Geophysics and Volcanology (INGV) Napoli, Italy) and the anonymous reviewer for their insightful comments on our original submission that improved the quality of the study.

Appendix A. Nonlinear Modelling

We simulate the nonlinear response of the archetype school building via 2D numerical models developed using OpenSees [48,49]. To account for the response of the building in different directions, we develop a 2D model for Frame 3-3 in the longitudinal direction and another for Frame B–B in the transverse direction, as indicated in Fig. 4. A lumped plasticity approach is adopted to simulate the nonlinear response of beams and columns by using zero-length rotational springs assigned at the ends of each element, as illustrated in Fig. 15a. Both diaphragms and beam-column joints are considered rigid. Gravity actions are modelled as uniformly distributed loads over the beam elements, whereas the masses are concentrated at the joint zones. A 5% Rayleigh damping ratio is assigned to the first two modes consistently with the approach proposed in [86], given that the hysteretic energy dissipation provides additional damping.

The nonlinear hysteretic response assigned to the zero-length rotational spring is described by the moment-rotation ($M-\theta$) model developed in [87], which has the advantage of addressing the degradation of strength and stiffness during both loading and unloading phases, amongst other models. The main parameters of the $M-\theta$ backbone curve are the effective initial stiffness K_e, yield moment M_y, yield rotation θ_y, hardening stiffness K_s, maximum moment M_c, capping rotation θ_{cap}, post-capping degrading stiffness K_c, and post-capping rotation θ_{pc}. The cyclic deterioration is evaluated using the normalised hysteretic energy dissipation parameter λ [87]. The parameters are quantified following [88], which derived mathematical formulations based on cyclic and monotonic experimental tests of 255 columns that failed either in flexural or flexural-shear modes.

The influence of masonry infill walls is addressed by modelling them as equivalent diagonal struts connected between beam-column joints, as observed in Fig. 15b. The force-deformation relationship assigned to the struts is defined per the backbone curve developed in [89]. The main parameters of this curve are the uncracked stiffness K_{mf}, strength at the first crack H_{mf}, displacement at the first crack u_f, secant stiffness at complete cracking K_{mfc}, strength at full cracking H_{mfc}, displacement at complete cracking u_{fc}, residual strength H_{mr}, and residual displacement u_r. The value of H_{mfc} represents the minimum strength among four different potential failure modes, i.e., sliding shear, diagonal tension, corner crushing and diagonal compression [89]. These parameters are then input to the '*Hysteretic*' material available in OpenSees, which is assigned to the equivalent diagonal struts for addressing the effect of infills on the global performance of the archetype school building. The factors that account for the degradation, pinching, and shape of cycles in the '*Hysteretic*' material are derived from [47] based on the results of experimental tests of infills.

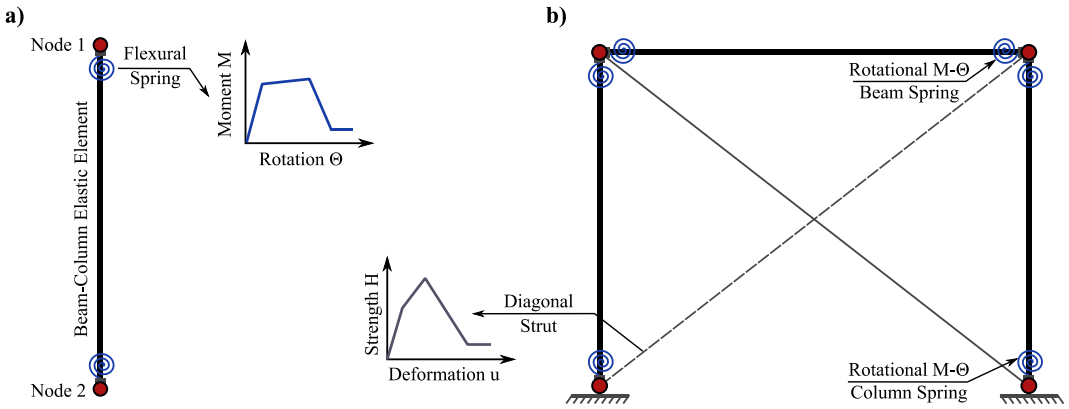

Fig. 15. (a) Modelling strategy for a column element; and (b) modelling of an infilled frame configuration.

Large windows generally characterise school buildings, especially in classrooms. Such openings can considerably influence the response of infills as they reduce their stiffness and lateral strength. To account for these effects, the strength parameters of the backbone curve of the infill are reduced using the factor (ρ) proposed in [90], which was calibrated based on the results of 84 experimental tests and 63 numerical tests of infilled frames with openings. This factor relies on window geometry with respect to the infill wall and the reinforcement conditions around window openings. It is assumed that the windows in the archetype school building have a width of 2.5 *m* in the longitudinal direction and 2.9 *m* in the transverse direction, with a height of 1.0 *m* in both directions.

Appendix B. Ground-motion Record Selection

The MSA approach adopted in this study requires the selection of hazard-consistent ground-motion records. We select ground-motion sets using the HaselREC [*Hazard-based SELection of RECords*] software [91], an open-source Python-based tool[11] which selects ground motion records according to the conditional spectrum (CS) approach proposed in [92]. The CS is a response spectrum that specifies the probability distribution of spectral accelerations over a range of periods of vibration, conditioned on a target spectral acceleration value at a conditioning period of interest. The CS approach uses the correlations between spectral accelerations at different periods to compute the expected (logarithmic mean) response spectrum and additionally account for the variability (variance) of the response spectra.

HaselREC performs ground-motion record selection using a target spectrum conditioned on a target value of the average spectral acceleration, AvgSA (i.e., the geometric mean of spectral acceleration values over a range of periods [93]), rather than on a single period of interest (e.g., Sa (T_1)). To compute the CS, haselREC requires the results from PSHA and hazard disaggregation analysis performed externally by the OpenQuake engine [94]. More details on the PSHA, hazard disaggregation, and record selection are provided in the following sections.

B1. PSHA and hazard disaggregation for Patras

We perform site-specific PSHA and hazard disaggregation analysis at the coordinates representative of the city of Patras (21.73457°N, 38.24664°E). We use the 2013 Euro-Mediterranean Seismic Hazard Model (ESHM13; [95]), for which data are freely available in OpenQuake format from the EFEHR website.[12] We compute seismic hazard for seven return periods of interest, ranging from 30 to 4995 years (namely 30, 98, 225, 475, 975, 2,475, and 4995 years). A representative V_{s30} value of 350 m/s is adopted. The selected IM is AvgSa, which is calculated by considering the period range between $0.2T_1$ and $2.0T_1$ to account for both higher modes and period elongation (e.g., [40,96]). Since the archetype school models are characterised by an infilled configuration, they might undergo up to $3-4T_1$ of period elongation due to the loss of lateral stiffness associated with infill damage [97]. To account for this issue, it is possible to define AvgSA using a T_1 representing the bare-frame configurations, i.e., $T_1 = 0.4$ s (e.g., [52]). Accordingly, the period range to compute AvgSa is [0.08s–0.80s]. We compute the standard deviation of AvgSa predictions per the correlation model in [98], for all GMMs considered in the ESHM13 ground-motion logic tree except [99], for which we use the European correlation model in [100]. The AvgSa values from the PSHA of Patras are provided in Table 10.

[11] https://github.com/elisa82/haselREC.
[12] http://www.efehr.org/en/home/.

Table 10
AvgSa values from the PSHA of Patras (full logic tree).

Return Period	AvgSa [g]
30	0.212
98	0.413
225	0.631
475	0.905
975	1.252
2475	1.852
4995	2.445

We perform hazard disaggregation [101] to define design earthquakes, i.e., the magnitude-distance pairs that contribute most to the seismic hazard at the selected site. We adopt the most representative branch of the ESHM13 logic tree for the disaggregation. This branch corresponds to the area source model that has the largest weight in the proposed source logic tree framework, and to the GMM in [99,102,103] for active tectonic and stable continental regions, subduction zones and volcanic regions, respectively. The mean moment magnitude and the Joyner-Boore distance obtained from the disaggregation analysis are provided in Table 11.

Table 11
Mean magnitude and distance from the disaggregation analysis (representative branch of the logic tree)

Return Period	Mean Magnitude	Mean Distance [km]
30	6.22	41.63
98	6.41	30.64
225	6.58	27.68
475	6.74	27.49
975	6.88	29.02
2475	7.07	33.36
4995	7.22	38.50

Note that AvgSa is adopted in this study only for carrying out PSHA, hazard disaggregation, and record selection. It is otherwise approximated by the spectral acceleration at the structure's fundamental period (Sa (T_1)), which can be more easily estimated in real-time through various EEW algorithms (e.g.,[104,105]).

B2. Ground-motion record selection

The spectral accelerations listed in Table 10 and the design earthquakes defined in Table 11 are used to compute the simplified CS in haselREC, along with the most representative GMM associated with the tectonic regime of dominant earthquakes (i.e., the GMM in [99]). We use a normal focal mechanism and a depth of 13 km to be consistent with the area source model of ESHM13. We perform ground-motion record selection for the same seven return periods of interest and the IM considered for PSHA, for a total of 7 record sets to be selected.

HaselREC relies on a composite database of response spectra (expressed as *RotD50* component, i.e., the median value of spectral accelerations computed over all rotation angles for a given ground motion; [106]), including the PEER (Pacific Earthquake Engineering Research Center) NGA-WEST2 [107] and the ESM (Engineering Strong Motion [108] database flatfiles. HaselREC allows a user to define screening criteria for the records to be considered for selection. These criteria are the maximum scaling factors (SFs), the V_{s30} range, and the Eurocode 8 soil class (to be used in conjunction with the data from the ESM database, for which V_{s30} is not always available), magnitude and distance ranges, and focal depth range. If both V_{s30} and Eurocode 8 soil class criteria are specified, V_{s30} is used. The magnitude and distance ranges are defined as intervals (i.e., radii) centred on the respective mean values from the disaggregation analysis. Only free-field ground motions are retained, to avoid the influence of the structure on the ground motion record.

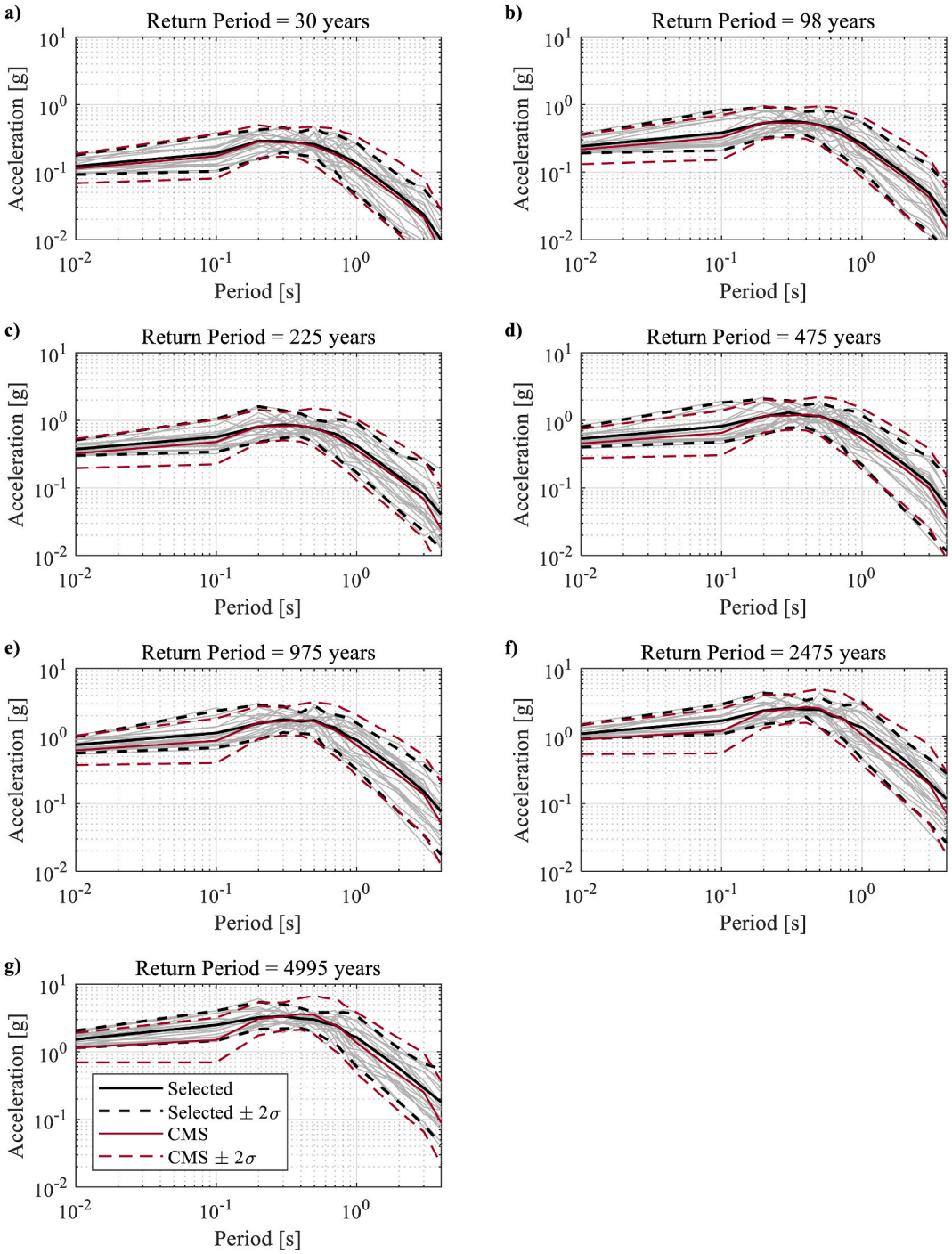

Fig. 16. Conditional mean spectra (CMS) and response spectra of the selected ground motions for the different return periods considered in this study (a) 30 years (b) 98 years (c) 225 years (d) 475 years (e) 975 years (f) 2475 years (g) 4995 years. Grey lines represent the RotD50 response spectra of selected ground motions, while black lines represent their distribution. The red lines represent the target conditional (mean) spectrum. Solid lines: mean (average) spectrum, dashed lines: mean spectrum values ± 2 standard deviations.

This study's V_{s30} values range between 200 m/s and 600 m/s [69]. The Eurocode 8 soil classes are chosen accordingly (i.e., only B and C soil classes are allowed). Only recordings from shallow crustal earthquakes (maximum focal depth = 30 km) are considered. The magnitude and distances radii and maximum allowable scaling factors are defined as a function of the return period. The adopted values are listed in Table 12.

Table 12
Parameters for ground motion record selection in Patras.

Return Period	Magnitude Radius	Distance Radius [km]	Maximum Allowable SF
30	0.50	50	2.0
98	0.50	50	2.5
225	0.50	50	2.5
475	0.75	75	3.5
975	1.00	100	4.5
2475	1.25	125	5.0
4995	1.50	150	5.0

For each return period, we select 20 two-component records. The results of the ground-motion selection are plotted in Fig. 16. It can be seen that the average spectrum of the selected recordings matches well with the conditional mean spectra (CMS) over the period range used to compute AvgSa (i.e., 0.08s–0.80s). The mean spectra plus/minus two standard deviations are also plotted to evaluate the dispersion of the selected ground motions with respect to the variability associated with the target CS. Agreement in this context is satisfactory in the range of periods of interest, especially at the lowest return periods. A summary of the SFs (average, minimum, maximum) associated with all the selections is provided in Table 13 as a function of the return period.

Table 13
Scaling factors (SF) adopted for record selection.

Return Period	Average SF	Minimum SF	Maximum SF
30	1.15	0.59	1.83
98	1.53	0.52	2.34
225	1.69	0.81	2.48
475	2.36	1.17	3.47
975	2.96	0.88	4.41
2475	3.58	1.02	4.90
4995	3.63	1.09	4.95

References

[1] J.D. Goltz, Introducing earthquake early warning in California : a summary of social science and public policy issues, in: A Report to OES and the Operational Areas, 2002 (Pasadena, California).
[2] J.A. Strauss, R.M. Allen, Benefits and costs of earthquake early warning, Seismol Res. Lett. 87 (2016) 765–772, https://doi.org/10.1785/0220150149.
[3] D.J. Wald, Practical limitations of earthquake early warning, Earthq. Spectra 36 (2020) 1412–1447, https://doi.org/10.1177/8755293020911388.
[4] G. Cremen, C. Galasso, Earthquake early warning: recent advances and perspectives, Earth Sci. Rev. 205 (2020), 103184, https://doi.org/10.1016/j.earscirev.2020.103184.
[5] F. Freddi, C. Galasso, G. Cremen, et al., Innovations in earthquake risk reduction for resilience: recent advances and challenges, Int. J. Disaster Risk Reduc. 60 (2021), 102267, https://doi.org/10.1016/j.ijdrr.2021.102267.
[6] I. Iervolino, V. Convertito, M. Giorgio, et al., Real-time risk analysis for hybrid earthquake early waring systemts, J. Earthq. Eng. 10 (2006) 867–885, https://doi.org/10.1080/13632460609350621.
[7] I. Iervolino, M. Giorgio, C. Galasso, G. Manfredi, Uncertainty in early warning predictions of engineering ground motion parameters: what really matters? Geophys. Res. Lett. 36 (2009) https://doi.org/10.1029/2008GL036644.
[8] G. Cremen, C. Galasso, A decision-making methodology for risk-informed earthquake early warning, Comput Civ Infrastruct Eng 36 (2021) 747–761, https://doi.org/10.1111/mice.12670.
[9] G. Cremen, C. Galasso, E. Zuccolo, Investigating the potential effectiveness of earthquake early warning across Europe, Nat. Commun. 13 (1) (2022) 639, https://doi.org/10.1038/s41467-021-27807-2.
[10] J. Moehle, G.G. Deierlein, A framework methodology for performance-based earthquake engineering, in: 13 Th World Conf Earthq Eng 13, 2004.
[11] I. Iervolino, Performance-based earthquake early warning, Soil Dynam. Earthq. Eng. 31 (2011) 209–222, https://doi.org/10.1016/j.soildyn.2010.07.010.
[12] O. Velazquez, G. Pescaroli, G. Cremen, C. Galasso, A review of the technical and socio-organizational components of earthquake early warning systems, Front. Earth Sci. 8 (2020), https://doi.org/10.3389/feart.2020.533498.
[13] M. Wyss, F. Wenzel, J. Daniell, in: F. Wenzel, J. Zschau (Eds.), How Useful Is Early Warning and Can it Be Made More Effective? BT - Early Warning for Geological Disasters: Scientific Methods and Current Practice, Springer Berlin Heidelberg, Berlin, Heidelberg, 2014, pp. 369–379.
[14] M. Motosaka, M. Homma, Earthquake early warning system application for school disaster prevention, J. Disaster Res. 4 (2009) 557–564, https://doi.org/10.20965/jdr.2009.x0557.
[15] M. Picozzi, A. Emolo, C. Martino, et al., Earthquake early warning system for schools: a feasibility study in southern Italy, Seismol Res. Lett. 86 (2015) 398–412, https://doi.org/10.1785/0220140194.
[16] B.-R. Wu, N.-C. Hsiao, P.-Y. Lin, et al., An integrated earthquake early warning system and its performance at schools in Taiwan, J. Seismol. 21 (2017) 165–180, https://doi.org/10.1007/s10950-016-9595-3.
[17] T. Hsu, C. Kuo, H. Wang, et al., The realization of an earthquake early warning system for schools and its performance during the 2019 ML 6.3 hualien (taiwan) earthquake, Seismol Res. Lett. 92 (2020) 342–351, https://doi.org/10.1785/0220190329.
[18] A. Emolo, M. Picozzi, G. Festa, et al., Earthquake early warning feasibility in the Campania region (southern Italy) and demonstration system for public school buildings, Bull. Earthq. Eng. 14 (2016) 2513–2529, https://doi.org/10.1007/s10518-016-9865-z.
[19] C.A. Cardno, Android phones now offer earthquake detection, Alerts. Civ Eng Mag 90 (2020) 34–36, https://doi.org/10.1061/ciegag.0001543.
[20] USGS EROS, Shuttle Radar Topography Mission (SRTM) 1 Arc-Second Global, 2018, https://doi.org/10.5066/F7PR7TFT.
[21] R. Caputo, A. Chatzipetros, S. Pavlides, S. Sboras, The Greek database of seismogenic sources (GreDaSS): state-of-the-art for northern Greece, Ann. Geophys. 55 (2012) 859–894, https://doi.org/10.4401/ag-5168.

[22] National Observatory of Athens, National Observatory of Athens Seismic Network, 1975, https://doi.org/10.7914/SN/HL.
[23] Aristotle University of Thessaloniki, Aristotle University of Thessaloniki Seismological Network (1981), https://doi.org/10.7914/SN/HT.
[24] University of Patras, University of Patras, Seismological Laboratory, 2000, https://doi.org/10.7914/SN/HP.
[25] University of Athens, Hellenic Seismological Network, University of Athens, Seismological Laboratory, 2008, https://doi.org/10.7914/SN/HA.
[26] Institute of Engineering Seimology Earthquake Engineering, ITSAK Strong Motion Network, 1981, https://doi.org/10.7914/SN/HI.
[27] Corinth Rift Laboratory, RESIF datacenter, CL - Corinth Rift Laboratory seismological network (CRLNET), RESIF - Réseau Sismologique et géodésique Français (2013), https://doi.org/10.15778/resif.cl.
[28] M. Brooks, J.E. Clews, N.S. Melis, J.R. Underhill, Structural development of Neogene basins in western Greece, Basin Res. 1 (1988) 129–138, https://doi.org/10.1111/j.1365-2117.1988.tb00010.x.
[29] N.S. Melis, M. Brooks, R.G. Pearce, A microearthquake study in the Gulf of Patras region, western Greece, and its seismotectonic interpretation, Geophys. J. Int. 98 (1989) 515–524, https://doi.org/10.1111/j.1365-246X.1989.tb02286.x.
[30] N.S. Melis, P.W. Burton, M. Brooks, Coseismic crustal deformation from microseismicity in the Patras area, western Greece, Geophys. J. Int. 122 (1995) 815–836, https://doi.org/10.1111/j.1365-246X.1995.tb06840.x.
[31] P. Albini, A. Rovida, O. Scotti, H. Lyon-Caen, Large eighteenth–nineteenth century earthquakes in western Gulf of Corinth with reappraised size and location, Bull. Seismol. Soc. Am. 107 (2017) 1663–1687, https://doi.org/10.1785/0120160181.
[32] G.P. Mavroeidis, Y. Ding, N. Moharrami, Revisiting the 1995 MW 6.4 Aigion, Greece, earthquake: simulation of broadband strong ground motion and site response analysis, Soil Dynam. Earthq. Eng. 104 (2018) 156–173, https://doi.org/10.1016/j.soildyn.2017.08.023.
[33] G.-A. Tselentis, N.S. Melis, E. Sokos, K. Papatsimpa, The Egion June 15, 1995 (6.2M L) earthquake, western Greece, Pure Appl. Geophys. 147 (1996) 83–98, https://doi.org/10.1007/BF00876437.
[34] M.N. Fardis, F.V. Karantoni, A. Kosmopoulos, Statistical Study of Damage Due to Aegion Earthquake of 15-6-95, Report to Earthquake Planning and Protection Organization, 1997, 1997 (in Greek).
[35] G. Koukis, N. Sabatakakis, G. Tsiambaos, N. Katrivesis, Engineering geological approach to the evaluation of seismic risk in metropolitan regions: case study of Patras, Greece, Bull. Eng. Geol. Environ. 64 (2005) 219–235, https://doi.org/10.1007/s10064-005-0273-x.
[36] K.I. Konstantinou, N.S. Melis, S.-J. Lee, et al., Rupture process and aftershocks relocation of the 8 June 2008 Mw 6.4 earthquake in northwest peloponnese, western Greece, Bull. Seismol. Soc. Am. 99 (2009) 3374–3389, https://doi.org/10.1785/0120080301.
[37] V. Papazachos, K. Papazachou, The Earthquakes of Greece, Editions Ziti, Thessaloniki, 1997.
[38] van Hinsbergen Djj, D.G. van der Meer, W.J. Zachariasse, J.E. Meulenkamp, Deformation of western Greece during Neogene clockwise rotation and collision with Apulia, Int. J. Earth Sci. 95 (2005) 463, https://doi.org/10.1007/s00531-005-0047-5.
[39] E.A. Opabola, C. Galasso, T. Rossetto, et al., A mixed-mode data collection approach for building inventory development: Application to school buildings in Central Sulawesi, Indonesia, Earthquake Spectra 38 (4) (2022) 2901–2921, https://doi.org/10.1177/87552930221110256.
[40] EN 1998-1, Eurocode 8: Design of Structures for Earthquake Resistance - Part 1 : General Rules, Seismic Actions and Rules for Buildings [Authority: the European Union Per Regulation 305/2011, Directive 98/34/EC, Directive 2004/18/EC], 2004 (Brussels).
[41] G.A. Tselentis, L. Danciu, Probabilistic seismic hazard assessment in Greece - Part 1: engineering ground motion parameters, Nat. Hazards Earth Syst. Sci. 10 (2010) 25–39, https://doi.org/10.5194/nhess-10-25-2010.
[42] G.M. Calvi, D. Bolognini, Seismic response of reinforced concrete frames infilled with weakly reinforced masonry panels, J. Earthq. Eng. 5 (2001) 153–185, https://doi.org/10.1080/13632460109350390.
[43] EN 1992-1-1, Eurocode 2: Design of Concrete Structures - Part 1-1 : General Rules and Rules for Buildings, 2004 (Brussels).
[44] M.T. De Risi, C. Del Gaudio, P. Ricci, G.M. Verderame, In-plane behaviour and damage assessment of masonry infills with hollow clay bricks in RC frames, Eng. Struct. 168 (2018) 257–275, https://doi.org/10.1016/j.engstruct.2018.04.065.
[45] C. Del Gaudio, M.T. De Risi, P. Ricci, G.M. Verderame, Empirical Drift-Fragility Functions and Loss Estimation for Infills in Reinforced Concrete Frames under Seismic Loading, Springer Netherlands, 2019.
[46] K. Sassun, T.J. Sullivan, P. Morandi, D. Cardone, Characterising the in-plane seismic performance of infill masonry, Bull New Zeal Soc Earthq Eng 49 (2016) 98–115, https://doi.org/10.5459/bnzsee.49.1.98-115.
[47] N. Mohammad Noh, L. Liberatore, F. Mollaioli, S. Tesfamariam, Modelling of masonry infilled RC frames subjected to cyclic loads: state of the art review and modelling with OpenSees, Eng. Struct. 150 (2017) 599–621, https://doi.org/10.1016/j.engstruct.2017.07.002.
[48] S. Mazzoni, F. Mckenna, M.H. Scott, G.L. Fenves, Command Language Manual, 2003.
[49] F. McKenna, OpenSees: a framework for earthquake engineering simulation, Comput. Sci. Eng. 13 (2011) 58–66, https://doi.org/10.1109/MCSE.2011.66.
[50] Fema, Seismic Performance Assessment of Buildings: Volume 1 - Methodology, 2018 (Washington, DC).
[51] F. Jalayer, R. De Risi, G. Manfredi, Bayesian Cloud Analysis: efficient structural fragility assessment using linear regression, Bull. Earthq. Eng. 13 (2015) 1183–1203, https://doi.org/10.1007/s10518-014-9692-z.
[52] K. Aljawhari, R. Gentile, F. Freddi, C. Galasso, Effects of ground-motion sequences on fragility and vulnerability of case-study reinforced concrete frames, Bull. Earthq. Eng. (2020), https://doi.org/10.1007/s10518-020-01006-8.
[53] K. Aljawhari, R. Gentile, C. Galasso, A fragility-oriented approach for seismic retrofit design, Earthq. Spectra 38 (2022) 1813–1843, https://doi.org/10.1177/87552930221078324.
[54] EN 1998-3, Eurocode 8: Design of Structures for Earthquake Resistance – Part 3: Assessment and Retrofitting of Buildings [Authority: the European Union Per Regulation 305/2011, Directive 98/34/EC, Directive 2004/18/EC], 2005 (Brussels).
[55] F. Jalayer, C.A. Cornell, Alternative non-linear demand estimation methods for probability-based seismic assessments, Earthq. Eng. Struct. Dynam. 38 (2009) 951–972, https://doi.org/10.1002/eqe.876.
[56] J.W. Baker, Efficient analytical fragility function fitting using dynamic structural analysis, Earthq. Spectra 31 (2015) 579–599, https://doi.org/10.1193/021113EQS025M.
[57] E. Zuccolo, G. Cremen, C. Galasso, Comparing the performance of regional earthquake early warning algorithms in Europe, Front. Earth Sci. 9 (2021), https://doi.org/10.3389/feart.2021.686272.
[58] G. Cremen, E. Zuccolo, C. Galasso, Accuracy and uncertainty analysis of selected methodological approaches to earthquake early warning in Europe, Seismol Res. Lett. 92 (2021) 2321–2332, https://doi.org/10.1785/0220200414.
[59] D. Giardini, J. Wossner, L. Danciu, Mapping Europe's Seismic Hazard, vol. 95, Eos, Washington DC, 2014.
[60] R. Basili, V. Kastelic, W.P.3 Share, 2 Team, D3.4 - database of active faults and seismogenic sources, SHARE Project Grant Agreement no. 226967 (2011). Deliverable D3.4.
[61] D. Giardini, J. Woessner, L. Danciu, et al., Seismic Hazard Harmonization in Europe (SHARE): Online Data Resource, 2013, https://doi.org/10.12686/SED-00000001-SHARE.
[62] P.M. Mai, P. Spudich, J. Boatwright, Hypocenter locations in finite-source rupture models, Bull. Seismol. Soc. Am. 95 (2005) 965–980, https://doi.org/10.1785/0120040111.
[63] TURNkey Project, Deliverable 3.8: Software and accompanying report on improved procedures for rapid mapping of earthquake shaking, including adjustment factors for local site effects (RRE) (2021).
[64] E. Delavaud, F. Scherbaum, N. Kuehn, T. Allen, Testing the global applicability of ground-motion prediction equations for active shallow crustal regions, Bull. Seismol. Soc. Am. 102 (2012) 707–721, https://doi.org/10.1785/0120110113.
[65] G. Lanzano, L. Luzi, V. D'Amico, et al., Ground motion models for the new seismic hazard model of Italy (MPS19): selection for active shallow crustal regions and subduction zones, Bull. Earthq. Eng. 18 (2020) 3487–3516, https://doi.org/10.1007/s10518-020-00850-y.
[66] G. Cremen, M.J. Werner, B. Baptie, A new procedure for evaluating ground-motion models, with application to hydraulic-fracture-induced seismicity in the United Kingdom, Bull. Seismol. Soc. Am. 110 (2020) 2380–2397, https://doi.org/10.1785/0120190238.

[67] M. Kowsari, B. Halldorsson, B. Hrafnkelsson, et al., Calibration of ground motion models to Icelandic peak ground acceleration data using Bayesian Markov chain Monte Carlo simulation, Bull. Earthq. Eng. 17 (2019) 2841–2870, https://doi.org/10.1007/s10518-019-00569-5.
[68] E.M. Thompson, C. Worden, Estimating rupture distances without a rupture, Bull. Seismol. Soc. Am. 10 (2017) 1–9, https://doi.org/10.1785/0120170174.
[69] G. Giannaraki, N.S. Melis, Z. Roumelioti, Seismic Risk Assessment at TURNkey TB4 Using a Common Earthquake Scenario: an Application to Patras City and Aigion Town, Central Greece. 370, 2021 abstract – oral presentation, session 18, ESC2021, Corfu, Greece.
[70] J.P. Stewart, N. Klimis, A. Savvaidis, et al., Compilation of a local VS profile database and its application for inference of VS30 from geologic- and terrain-based proxies, Bull. Seismol. Soc. Am. 104 (2014) 2827–2841, https://doi.org/10.1785/0120130331.
[71] A.B. Batilas, Urban Accelerograph Network of Patras (UPAN): Installation, Database Development and Recording Process, Department of Civil Engineering, Laboratory of Geotechnical Engineering, University of Patras, 2015. PhD dissertation.
[72] H.P. Crotwell, T.J. Owens, J. Ritsema, The TauP Toolkit: flexible seismic travel-time and ray-path utilities, Seismol Res. Lett. 70 (1999) 154–160, https://doi.org/10.1785/gssrl.70.2.154.
[73] B.L.N. Kennett, E.R. Engdahl, Traveltimes for global earthquake location and phase identification, Geophys. J. Int. 105 (1991) 429–465, https://doi.org/10.1111/j.1365-246X.1991.tb06724.x.
[74] A. Rigo, H. Lyon-Caen, R. Armijo, et al., A microseismic study in the western part of the Gulf of Corinth (Greece): implications for large-scale normal faulting mechanisms, Geophys. J. Int. 126 (1996) 663–688, https://doi.org/10.1111/j.1365-246X.1996.tb04697.x.
[75] D.T. Trugman, M.T. Page, S.E. Minson, E.S. Cochran, Peak ground displacement saturates exactly when expected: implications for earthquake early warning, J. Geophys. Res. Solid Earth 124 (2019) 4642–4653, https://doi.org/10.1029/2018JB017093.
[76] R.M. Allen, in: P. Gasparini, G. Manfredi, J. Zschau (Eds.), The ElarmS Earthquake Early Warning Methodology and Application across California BT - Earthquake Early Warning Systems, Springer Berlin Heidelberg, Berlin, Heidelberg, 2007, pp. 21–43.
[77] Y. Behr, J. Clinton, P. Kästli, et al., Anatomy of an earthquake early warning (EEW) alert: predicting time delays for an end-to-end EEW system, Seismol Res. Lett. 86 (2015) 830–840, https://doi.org/10.1785/0220140179.
[78] Y.-M. Wu, H. Kanamori, Experiment on an onsite early warning method for the taiwan early warning system, Bull. Seismol. Soc. Am. 95 (2005) 347–353, https://doi.org/10.1785/0120040097.
[79] H. Kanamori, REAL-TIME seismology and earthquake damage mitigation, Annu. Rev. Earth Planet Sci. 33 (2005) 195–214, https://doi.org/10.1146/annurev.earth.33.092203.122626.
[80] M. Bracale, S. Colombelli, L. Elia, et al., Design, implementation and testing of a network-based earthquake early warning system in Greece, Front. Earth Sci. 9 (2021), https://doi.org/10.3389/feart.2021.667160.
[81] G.J. O'Reilly, D. Perrone, M. Fox, et al., Seismic assessment and loss estimation of existing school buildings in Italy, Eng. Struct. 168 (2018) 142–162, https://doi.org/10.1016/j.engstruct.2018.04.056.
[82] A. Silva, J.M. Castro, R. Monteiro, A rational approach to the conversion of FEMA P-58 seismic repair costs to Europe, Earthq. Spectra 36 (2020) 1607–1618, https://doi.org/10.1177/8755293019899964.
[83] D. Cardone, G. Perrone, Developing fragility curves and loss functions for masonry infill walls, Earthq Struct 9 (2015) 257–279, https://doi.org/10.12989/eas.2015.9.1.257.
[84] D. Cardone, G. Perrone, Damage and loss assessment of pre-70 RC frame buildings with FEMA P-58, J. Earthq. Eng. 21 (2017) 23–61, https://doi.org/10.1080/13632469.2016.1149893.
[85] A. Silva, L. Macedo, R. Monteiro, J.M. Castro, Earthquake-induced loss assessment of steel buildings designed to Eurocode 8, Eng. Struct. 208 (2020), https://doi.org/10.1016/j.engstruct.2020.110244.
[86] F. Zareian, R.A. Medina, A practical method for proper modeling of structural damping in inelastic plane structural systems, Comput. Struct. 88 (2010) 45–53, https://doi.org/10.1016/j.compstruc.2009.08.001.
[87] L.F. Ibarra, R.A. Medina, H. Krawinkler, Hysteretic models that incorporate strength and stiffness deterioration, Earthq. Eng. Struct. Dynam. 34 (2005) 1489–1511, https://doi.org/10.1002/eqe.495.
[88] C.B. Haselton, A.B. Liel, S.C. Taylor-Lange, G.G. Deierlein, Calibration of model to simulate response of reinforced concrete beam-columns to collapse, ACI Struct. J. 113 (2016) 1141–1152, https://doi.org/10.14359/51689245.
[89] L. Liberatore, L.D. Decanini, Effect of infills on the seismic response of high-rise RC buildings designed as bare according to Eurocode 8 [Infl uenza della tamponatura sulla risposta sismica di edifi ci in c.a. alti progettati come nudi con l'Eurocodice 8], Ing Sismica 28 (2011) 7–23.
[90] L.D. Decanini, L. Liberatore, F. Mollaioli, Strength and stiffness reduction factors for infilled frames with openings, Earthq. Eng. Eng. Vib. 13 (2014) 437–454, https://doi.org/10.1007/s11803-014-0254-9.
[91] E. Zuccolo, G.J. O'Reilly, V. Poggi, R. Monteiro, haselREC: an automated open-source ground motion record selection and scaling tool, Bull. Earthq. Eng. 19 (2021) 5747–5767, https://doi.org/10.1007/s10518-021-01214-w.
[92] J.W. Baker, C. Lee, An improved algorithm for selecting ground motions to match a conditional spectrum, J. Earthq. Eng. 22 (2018) 708–723, https://doi.org/10.1080/13632469.2016.1264334.
[93] M. Kohrangi, P. Bazzurro, D. Vamvatsikos, A. Spillatura, Conditional spectrum-based ground motion record selection using average spectral acceleration, Earthq. Eng. Struct. Dynam. 46 (2017) 1667–1685, https://doi.org/10.1002/eqe.2876.
[94] M. Pagani, D. Monelli, G. Weatherill, et al., Openquake engine: an open hazard (and risk) software for the global earthquake model, Seismol Res. Lett. 85 (2014) 692–702, https://doi.org/10.1785/0220130087.
[95] J. Woessner, D. Laurentiu, D. Giardini, et al., The 2013 European Seismic Hazard Model: key components and results, Bull. Earthq. Eng. 13 (2015) 3553–3596, https://doi.org/10.1007/s10518-015-9795-1.
[96] M. Kohrangi, P. Bazzurro, D. Vamvatsikos, Vector and scalar IMs in structural response estimation, Part II: building demand assessment, Earthq. Spectra 32 (2016) 1525–1543, https://doi.org/10.1193/053115EQS081M.
[97] G.J. O'Reilly, M. Kohrangi, P. Bazzurro, R. Monteiro, Intensity measures for the collapse assessment of infilled RC frames, 16th Eur Conf Earthq Eng (2018).
[98] J. Baker, N. Jayaram, Correlation of spectral acceleration values from NGA ground motion models, Earthq Spectra - EARTHQ SPECTRA 24 (2008), https://doi.org/10.1193/1.2857544.
[99] S. Akkar, J.J. Bommer, Empirical equations for the prediction of PGA, PGV, and spectral accelerations in Europe, the mediterranean region, and the Middle East, Seismol Res. Lett. 81 (2010) 195–206, https://doi.org/10.1785/gssrl.81.2.195.
[100] S. Akkar, M.A. Sandikkaya, B. Ay, Compatible ground-motion prediction equations for damping scaling factors and vertical-to-horizontal spectral amplitude ratios for the broader Europe region, Bull. Earthq. Eng. 12 (2014), https://doi.org/10.1007/s10518-013-9537-1.
[101] P. Bazzurro, C.A. Cornell, Disaggregation of seismic hazard, Bull. Seismol. Soc. Am. 89 (1999) 501–520.
[102] J.X. Zhao, J. Zhang, A. Asano, et al., Attenuation relations of strong ground motion in Japan using site classification based on predominant period, Bull. Seismol. Soc. Am. 96 (2006) 898–913, https://doi.org/10.1785/0120050122.
[103] E. Faccioli, A. Bianchini, M. Villani, New ground motion prediction equations for T > 1 s and their influence on seismic hazard assessment, in: Proceedings of the University of Tokyo Symposium on Long-Period Ground Motion and Urban Disaster Mitigation, March 17-18, 2010, pp. 1–8.
[104] V. Convertito, I. Iervolino, A. Zollo, G. Manfredi, Prediction of response spectra via real-time earthquake measurements, Soil Dynam. Earthq. Eng. (2008), https://doi.org/10.1016/j.soildyn.2007.07.006.
[105] J. Fayaz, C. Galasso, A deep neural network framework for real-time on-site estimation of acceleration response spectra of seismic ground motions, Comput Civ Infrastruct Eng n/a (2022), https://doi.org/10.1111/mice.12830.

[106] D.M. Boore, Orientation-independent, nongeometric-mean measures of seismic intensity from two horizontal components of motion, Bull. Seismol. Soc. Am. 100 (2010) 1830–1835, https://doi.org/10.1785/0120090400.
[107] T.D. Ancheta, R.B. Darragh, J.P. Stewart, et al., NGA-West2 database, Earthq. Spectra 30 (2014) 989–1005, https://doi.org/10.1193/070913EQS197M.
[108] G. Lanzano, S. Sgobba, L. Luzi, et al., The pan-European Engineering Strong Motion (ESM) flatfile: compilation criteria and data statistics, Bull. Earthq. Eng. 17 (2019) 561–582, https://doi.org/10.1007/s10518-018-0480-z.
[109] ASCE, Minimum design loads and associated criteria for buildings and other structures, ASCE/SEI (2017) 7–16.
[110] G. Cremen, F. Bozzoni, S. Pistorio, C. Galasso, Developing a risk-informed decision-support system for earthquake early warning at a critical seaport, Reliab. Eng. Syst. Saf. 218 (2022), 108035, https://doi.org/10.1016/j.ress.2021.108035.